A NEURAL NETWORK TO DETECT MOTOR IMAGERY IN ECOG DATA RECORDED DURING DREAMING

Master Thesis

System Biology master program

Vilnius university

STUDENT NAME: Taisija Dėmčėnko
STUDENT NUMBER: 2011284

SUPERVISOR: Milena Korostenskaja

SUPERVISOR DECISION: .....

FINAL GRADE: .....

DATE OF SUBMISSION:

CONTENTS

LIST OF ABBREVIATIONS

ANN	Artificial Neural Network
BCI	Brain Machine Interface
CAR	Common Average Reference
CNN	Convolutional Neural Network
CSM	Cortical Stimulation Mapping
CWT	Continuous Wavelet Transform
ECoG	electrocorticography
EEG	electroencephalography
FFT	Fast Fourier Transform
fMRI	functional Magnetic Resonance Imaging
MEG	magnetoencephalography
ML	Machine Learning
MSE	mean squared error
NREM	non-Rapid Eye Movement
PCA	Principal Component Analysis
PET	positron emission tomography
PGO	ponto-geniculo-occipital
PSD	power spectral density
ReLU	Rectified Linear Unit
REM	Rapid Eye Movement
RTFM	real-time functional mapping
SGD	Stochastic Gradient Descent
tDCS	transcranial Direct Current Stimulation

INTRODUCTION

People spend about one third of their lives sleeping, and the absolute majority see dreams. Dreams impact our emotions and memory (Klinzing et al., 2019; Pagel & Kwiatkowski, 2003; Paller et al., 2021; Paul et al., 2015), and are relevant to neuroscience of consciousness (Caviglia, 2021; Fosse & Larøi, 2020; Hobson, 2009; Horton, 2017; C. Speth & Speth, 2018). However, most dreams are forgotten (Herlin et al., 2015). Even when remembered, there is a significant possibility that the memory about a dream was altered after awakening (Beaulieu-Prévost & Zadra, 2015; Hilditch & McHill, 2019), e.g. due to the mechanism of active dream forgetting (Izawa et al., 2019). A method to record dreams during sleeping can remove this barrier and help to pinpoint the role of dreaming, and to analyze dream contents more confidently in psychotherapy or clinics (Carr & Nielsen, 2015; Zadra & Domhoff, 2011).

During dreaming, brain activation is observed in humans and other animals and correlates with sensory, perceptual, and cognitive phenomena which happens in dreams (Blake et al., 2019; Dresler et al., 2011; Maquet, 2000; Siclari et al., 2017; Torontali et al., 2019). Still, brain activity patterns are not yet researched enough to be easily decoded into dream contents, which are described to be complex and multi-sensory (Carr & Nielsen, 2015; Fosse & Larøi, 2020; Martin et al., 2020; C. Speth & Speth, 2018). Moreover, it is difficult to verify whether brain activity patterns during specific wakeful experiences are the same as ones in dream experiences, as the same problem arises: the difficulty of accurate identification of dream experiences. Nevertheless, for lucid dreamers and patients with disrupted muscle atonia, brain activation patterns during motor imagery in dreaming corresponded to the motor imagery in a wakeful state (Dresler et al., 2011; Erlacher & Schredl, 2008; Mahowald & Schenck, 2011; Noreika et al., 2020; J. Speth & Speth, 2016). This means that motor imagery data can already be studied while developing a model to classify dream contents. There are already many studies on motor imagery classification, as it is commonly used in Brain Machine Interfaces (BCIs) for fully or partially paralyzed patients (Aydemir & Kayikçioğlu, 2010; Miller et al., 2020), though they are mostly based on unilateral or bilateral hand movements, while many types of movement imagery can be present in dreams, often simultaneously. The development of a multi-class deep learning model is needed to discriminate between many different movement types, and for that, a high resolution of data is needed.

Electrocorticography (ECoG) can provide significantly better spatial and temporal resolution than the more common electroencephalography (EEG) method (Haufe et al., 2018; Kaiju et al., 2017; Leuthardt et al., 2021). Because of that, ECoG has the potential to contain more information needed to pinpoint complex components such as emotions or visuals (Blakely et al., 2008; Cheng et al., 2019). However, ECoG data is rare and not generalized between subjects. Advancements in Machine Learning (ML) methods facilitate faster and easier data processing and feature extraction (Lu et al., 2017; Moon et al., 2018; RaviPrakash et al., 2020; Shen et al., 2019; Sun et al., 2020), but can overfit when the training data set is too small. This introduces significant difficulties in using ECoG data with deep ML models.

A way to generalize ECoG data to train a model on several subjects simultaneously is proposed in this work. It is a generic pipeline that benefits from incorporating spatial information into data sets, allows to change parameters of data transformation and model training on the fly, and makes possible the cross-testing of models trained on different data sets. This pipeline is used with an ECoG data set to develop a classifier that discriminates between hand and tongue movement from patients with differently placed ECoG grids. An emphasis is made on Convolutional Neural Network (CNN)

models, which are efficient with spatial features but are usually used on images. A hypothesis is tested on whether a motor imagery classifier can be trained on real motor data, as such data is easier to collect. Lastly, the model is applied on a different ECoG data set to predict motor imagery during Rapid Eye Movement (REM) sleep.

AIM AND TASKS

The purpose of this study was to develop a CNN based predictor to discriminate between movement imagery types in a continuous brain activity recording. This predictor is the prototype of a model which detects and decodes sleeping brain activation patterns. The tasks are:

1. Designing a data processing pipeline to include electrode location information into the data, which is useful both as a feature and for data standardization between patients;
2. Developing a ML model which classifies data fragments by motor imagery type, and comparing results between single-patient models and a model combining several patients;
3. Comparing results between models trained on imaginary and real motor data to assess whether the similarity is big enough to allow real motor experiments to collect data in the future;
4. Running the model on another data set recorded during the REM sleep, during which most dreaming happens, and speculate on relevance of results.

LITERATURE REVIEW

3.1 Dreams

3.1.1 Dream source and contents

It is believed that humans see dreams every night, but forget most of them (Herlin et al., 2015). Zadra and Domhoff (2011) define a dream to be a form of thinking during sleep when a certain minimal level of brain activation is observed, but the self-awareness is lost; it is experienced as a series of events resembling waking reality. Siclari et al. (2017) show that dreaming during sleep can be detected by an increase of high-frequency power and decrease of low-frequency power in posterior cortical regions, and that these changes happen in areas associated with functions reported later in dream reports. This further increases the similarity of dreaming and wakeful perceptions. On the other hand, a difference in signal temporal complexity can be used to distinguish between sleep and wakefulness (González et al., 2019). Dreams are also used in psychotherapy (Caviglia, 2021) and neuropsychological studies (Mota et al., 2014).

In healthy subjects, dreams only occur during sleeping. Sleep is currently differentiated into two main stages cycling between each other: REM, which is also sometimes called paradoxical sleep, and non-Rapid Eye Movement (NREM) (Rasch & Born, 2013). Most dreaming occurs during REM sleep, although some dreams are detected during NREM sleep (Carr & Nielsen, 2015). During the transition from wakefulness to NREM sleep, dreams are also possible and quite often, but mostly short or fragmentary (Hobson, 2009; Nir & Tononi, 2010). These dreams are called hypnagogic dreams and are often analyzed in dream studies, as they take less time to happen and are more easily controlled (Beaulieu-Prévost & Zadra, 2015; Haar Horowitz et al., 2020).

Carr and Nielsen (2015) compare the content of daydreaming, REM and NREM dreams and show that REM dreams are more emotional, have more bizarre and sensory experiences. Moreover, Martin et al. (2020) have shown that REM reports are more complex than NREM dreams. A state similar to dreaming, called "dreamy state", is observed in subjects during seizures from temporal lobe epilepsy (Vignal et al., 2007), or can be induced by stimulation of the amygdala (Lai et al., 2020). As the amygdala is thought to be one of main players in perceiving emotions, the high emotional load of dreams can be linked to the observed activation of amygdala during REM sleep (Blake et al., 2019; Maquet, 2000).

Characteristic phenomena of the REM sleep stage are ponto-geniculo-occipital (PGO) waves, which can be detected right before the start of REM sleep stage. PGO waves start in the pons and include the brainstem, lateral geniculate nucleus, and occipital cortex (Gott et al., 2017; Wang et al., 2021); in the occipital cortex, PGO waves reach the highest amplitude, especially in primary visual and visual association cortices (Eagleman & Vaughn, 2021; Frauscher et al., 2018), which is thought to be the source of vivid hallucinations during dreams.

During REM sleep, there is a high activation of motor cortex regions and other brain areas responsible for movement, such as cerebellum and basal ganglia (J. Speth & Speth, 2016). Despite that, muscle atonia is normal during the REM sleep stage, meaning that although body movements are commanded by the motor cortex, they are inhibited (Torontali et al., 2019; Valencia Garcia et al., 2018). Motor imagery is quite common in dreams (C. Speth & Speth, 2018; J. Speth & Speth, 2016), which can be reflected in real life when certain disorders disrupt muscle atonia (Barone & Henchcliffe, 2018). Moreover, the amount of motor imagery in dreams can be both increased (J. Speth & Speth,

2016) and decreased (Noreika et al., 2020) using transcranial Direct Current Stimulation (tDCS).

In subjects with loss of muscle atonia, movements produced during dreaming correspond with ones mentioned in dream reports collected afterwards (Mahowald & Schenck, 2011). Additionally, Dresler et al. (2011) show that predefined motor imagery can be detected in dreams of lucid dreamers. A similar conclusion was drawn earlier by Erlacher and Schredl (2008), although they point out studies showing some differences between dreamed and actual movements, like different time duration needed to perform the task. Still, this makes the movement imagery component of dreams available for detection in dream recordings with models trained on motor imagery during wakefulness.

3.1.2 Dream analysis and lucid dreaming

The sensory, perceptual, and cognitive phenomena in dreams are usually analyzed via dream reports, which are collected in different ways: laboratory awakenings, questionnaires, or home dream diaries (Zadra & Domhoff, 2011). The sleep stage can be detected in real-time by polysomnography, which is a set of recordings of biophysiological changes during sleep. Many dream studies resort to sleep stage detection with polysomnography (e.g. Frauscher et al., 2018; Herlin et al., 2015; Konkoly et al., 2021; Simor et al., 2012). Polysomnography examples of different signals during different wakefulness and sleep stages are visualized in Figure 3.1.

There is a significant problem with analyzing dream contents: studies depend on subjects' ability to remember and describe their dreams, which can lead to altered descriptions and introduce bias (Beaulieu-Prévost & Zadra, 2015; Herlin et al., 2015). Moreover, dream analysis becomes impossible for patients which cannot describe their dreams because of a specific disability or mental state. Dreams are also quickly forgotten (Izawa et al., 2019), so they need to be reported right after awakening, which is complicated by sleep inertia accompanied by poor cognitive performance (Hilditch & McHill, 2019). Moreover, other things can influence dream reports, such as the laboratory setting; method, time, and sleep stage of awakening; the instructions provided (Fosse & Larøi, 2020); socio-cognitive factors (some dream experiences happen rarer in a laboratory setting than at home); or subject personality (Carr & Nielsen, 2015; Zadra & Domhoff, 2011).

Some dream studies resort to lucid dreamers. A lucid dream is during which a person is aware that they dream, and can influence it. Lucid dreamers can be instructed to do specific eye movements after entering the state of lucidity, so the presence of dreaming can be recorded by an observer (see Fig. 3.2). It is estimated that once-a-month lucid dreamers make 20 % of the general population, and more frequent lucid dreaming is rare (Stumbrys et al., 2014). Although various techniques are developed to induce lucidity (Stumbrys et al., 2012), and even a two-way communication during dreaming is with

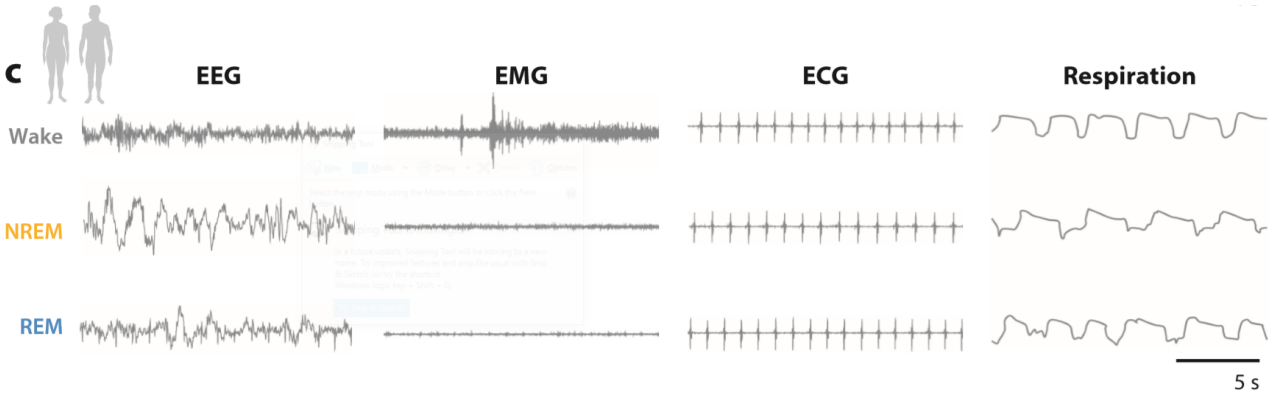

Figure 3.1: Examples of human polysomnography recordings during wakefulness, NREM sleep, and REM sleep. Source: D. Liu and Dan (2019).

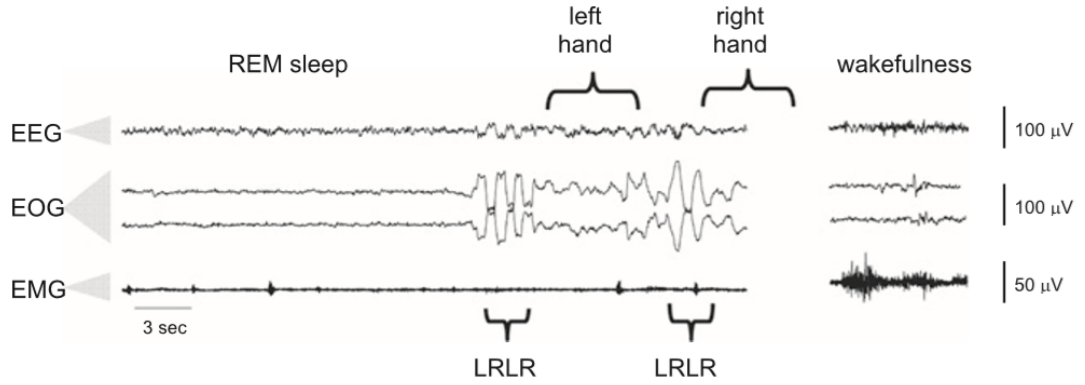

Figure 3.2: Changes in polysomnography oscillations detected during a lucid dreamer doing specific tasks while REM dreaming. LRLR means left-right-left-right eye movement. Source: Dresler et al. (2011).

lucid dreamers (Konkoly et al., 2021), there is no reliable way to induce lucidity anytime it is needed, and subjects still have difficulties in describing a dream. For instance, in Dresler et al. (2011) study, only two out of six experienced lucid dreamers were able to achieve lucidity and do the required task.

This leads to the conclusion that dream reports are not suitable for objectively studying dream perceptual and cognitive phenomena. The ability to decode dreaming contents directly from brain activity would be extremely valuable for consciousness and neuropsychology research. Moreover, the possibility of decoding dreams while they happen introduces a new type of therapy currently impracticable: affecting sleep and dreams right after detecting specific in-dream phenomena. For example, subjects with nightmare disorders could be awoken or affected in other ways when a nightmare starts, making them less susceptible to fear of sleeping and consequent sleep deprivation. Additionally, remembered dream content can impact the consequent wakefulness (Pagel & Kwiatkowski, 2003; Paller et al., 2021; Paul et al., 2015), but nothing is known about the contents of forgotten dreams, which nevertheless can affect the mood or actions of the person after awakening.

3.1.3 The reaDream project

This work is the first step towards the reaDream project: developing a system for decoding and visualizing human dream perceptual and cognitive phenomena directly from recorded brain activity. The reaDream concept consists of a recording device and a decoding model. The recording device uses ECoG technology to record brain electromagnetic activity while the user is sleeping. Recordings are transferred to an external device, like a personal computer or a smartphone, using wireless technology such as Wi-Fi. Dream decoding happens in real-time by a deep learning-based model (see learning scheme in Fig. 3.3(b)), which is stored on that external device. Text-based dream reports are generated and stored on the same external device. Later, these reports can be converted into videos or a Virtual Reality experience, which would allow one to re-experience the dream. Additionally, the model can learn to make certain decisions (e.g. waking the user), sending the instruction back to the recording device, if it has the brain stimulation function. This would make reaDream a closed-loop BCI (Caldwell et al., 2019), which would be useful in the therapy of certain disorders.

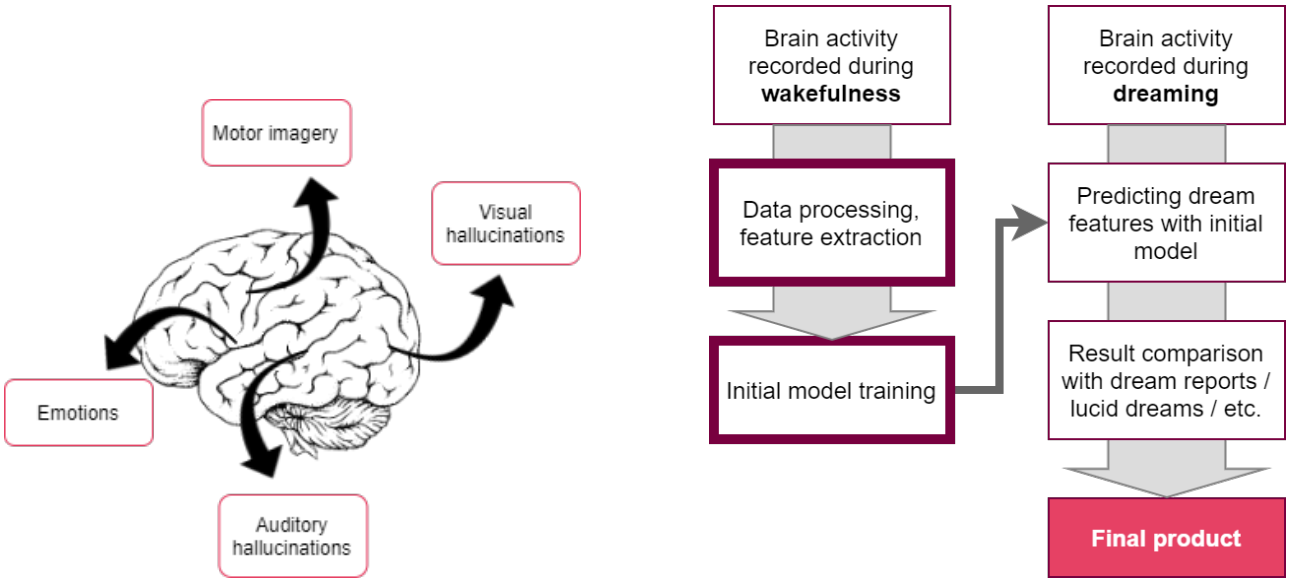

(a) (b)

Figure 3.3: The reaDream project. (a): four dream perceptual components from which the final report can be generated. (b): a simple scheme of training a model to produce correct dream reports.

Besides accurate dream decoding, a significant challenge for reaDream is to make the recording device safe and comfortable for everyday use in home conditions. As dreams are complex and multi-sensory, containing visions, auditory hallucinations, motor imagery, and emotions, a need may arise for electrode sets implanted in several different brain areas, some of which (e.g. amygdala) are quite deep in the brain. Although more research is needed to pinpoint brain areas crucial for decoding accurate and detailed dream reports, currently available recording technologies might be not safe enough to be used for such a task. Nevertheless, with the development of safer implantation routines and high-resolution recording technologies (Musk & Neuralink, 2019; Oxley et al., 2021), and the rising interest in BCI research, reaDream becomes feasible. Additionally, variousML models are developed to decode some of the perceptual components of interest; for instance, Horikawa et al. (2013) decoded visual imagery during sleep.

3.2 Brain activity

3.2.1 Brain structure and functions

The human brain consists of neurons, which communicate using electrochemical impulses, called action potentials. They travel through axons of neurons, and the signal is transferred to another neuron through a synapse. These signals are connected to the ability of the brain to execute various sophisticated functions. Studying neuron connections and activation patterns helps to understand how these functions are performed.

It is not feasible to measure the activity of each neuron, as there are more than 86 billion neurons in the human brain (Van Essen et al., 2019). Fortunately, it is not necessary, as neurons fire in groups. Because of the all-or-none principle of an action potential, recording a single neuron results in a spike train, while recording groups of neurons will return wavelike sums of spike trains, called local field potentials. Local field potentials can be recorded using non-invasive technology, which makes the recording easier with human subjects, although the spatial resolution is lost.

The cerebral cortex makes the most of the outer part of the brain and is also responsible for most

cognitive functions. Outer layers of the cerebral cortex consist of pyramidal cells aligned perpendicular to the cortex surface. A pyramidal cell is a type of neuron which is implicated in cognition. It has a typical conic cell body, a single axon, multiple basal dendrites, and a large apical dendrite with dendritic spines (Kanari et al., 2019). These numerous spines are accountable for the huge amount of inputs one pyramidal cell can receive, although not every dendritic contact forms an actual synapse (Holler et al., 2021). These facts make the cerebral cortex activity both valuable to research and relatively simple to record.

At the dawn of brain research, it was thought that brain functions are strictly happening in specific brain areas, also called neural circuits. Later, it has been shown that this is not always the case (Snyder et al., 2015). High-level cognitive processes can be the product of neural circuits, which connect into full-brain networks: for instance, emotions can be discriminated using connectivity patterns between channels placed in different brain areas (Cheng et al., 2019; Moon et al., 2018). Despite this, some functions are found to be confined to specific areas, such as speech production in Broca's area, speech comprehension in Wernicke's area (Jahangiri et al., 2021), or face recognition in the fusiform gyrus (Schalk et al., 2017). Nevertheless, Yellapantula et al. (2021) show the participation of distributed brain networks in language function, which agrees with the idea that high-level functions are a result of complex connections between many neural circuits.

Moreover, the brain changes throughout its lifetime to adjust to environmental changes. The ability of the brain to change its networks through growth and reorganization is called neuroplasticity. It is crucial for brain development and adaptation and has an impact on learning, memory, and recovery from brain damage. A common example is function transfer from one brain area to another, such as compensation of sensory loss by enhancing the perception of other sensory signals (Imbiriba et al., 2010; Voss et al., 2017). Consequently, each brain has unique connectivity, and differences between subjects' brains can be significant, making the generalization of human brain activity somewhat challenging. Neuroplasticity plays a crucial role in neuropathology, as brain functions can be affected by lesions or tumors. As a result, brain functional mapping for each patient is required.

Functional mapping is done to understand which brain areas take part in which functions. It is usually done in real-time for patients which require brain surgery. The current gold standard for real-time functional mapping (RTFM) is cortical stimulation mapping, which requires craniotomy, is time consuming, and has a potential to provoke seizures (Jahangiri et al., 2021); alternatively, RTFM can be done with cortical stimulation mapping while retaining relatively high accuracy (Hill et al., 2012; Kanaya et al., 2021; Korostenskaja et al., 2015; Prakash et al., 2017). During Cortical Stimulation Mapping (CSM), while an area is stimulated, its function is determined by the disability of the patient to perform certain actions (negative mapping), or inducing those actions involuntary (positive mapping). Additionally, ECoG grids are placed near the area of stimulation to record brain electrical activity and detect after-discharges or seizures (Jahangiri et al., 2021). On the other hand, ECoG-based RTFM is based on detecting changed activity in specific brain areas while the patient is performing a function.

Various methods were developed to find the strength of brain area activation or deactivation, usually by comparison of broadband power. The chosen frequency range for the analyzed broadband depends on the type and complexity of performed task: for example, language tasks are shown to be reflected in high gamma as a result of localized cortical processing (60 - 70 Hz and higher in Kanaya et al., 2021; Zheng et al., 2021), while initiation of any motor task can be detected by lower 8 - 32 Hz power (Miller et al., 2020).

3.2.2 Brain activation during motor imagery

The human motor cortex is a region of the frontal lobe anterior to the central sulcus, and consists of several parts: the primary motor cortex (Brodmann area 4), premotor cortex, and supplementary

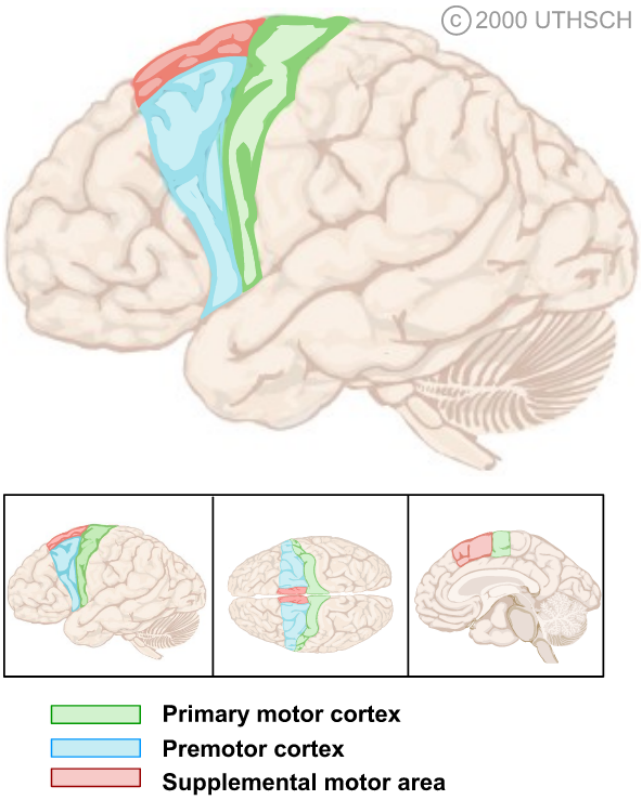

Figure 3.4: Motor cortex areas (lateral, dorsal, and medial views). Source: "Motor Cortex (Section 3, Chapter 3) Neuroscience Online: An Electronic Textbook for the Neurosciences | Department of Neurobiology and Anatomy - The University of Texas Medical School at Houston" (n.d.).

motor area (see Fig. 3.4). It was shown to be activated during the planning, control, and execution of movement. The premotor cortex and supplementary motor area encode higher-level movements compared to the primary motor cortex, which is associated with producing simple movements. Nevertheless, it was shown that the primary motor cortex also plays a role in motor imagery, although its activation magnitude is weaker compared to activation from actual movement (Batula et al., 2017; Miller et al., 2010).

Both hemispheres contain a motor cortex, which controls the opposite side of the body. However, motor cortex halves are asymmetric based on the subject's handiness (Pool et al., 2014). Additionally, movement of both hands, or bimanual movement, requires additional interactions between hemispheres, and brain activation during a bimanual movement is not just a sum of two independent movements (Choi et al., 2018).

Dahm and Rieger (2016) list several studies showing that imagination and execution of movement have similar activation duration and patterns, but during motor imagery without actual movement, the muscle should be inhibited, resulting in loss of movement feedback. This introduces a notable difference between imagery and actual motion for uncommon movements (e.g. non-dominant hand movements). This should be taken into consideration when talking about motor imagery in dreams, as it can be strongly different from the wakeful motion (e.g. flying).

There are plenty of studies on decoding commanded movements from brain activity, which is often used in BCIs. For instance, Miller et al. (2020) mention many ECoG-based BCIs which helped to move a cursor on a computer screen, type letters, and control limbs of an exoskeleton. Although most simple prostheses like bionic limbs work by detecting the signal in the muscle, the signal can be detected in the brain when the movement is only imagined. Often it is done by placing the electrodes over the

sensorimotor cortex and detecting increases in high-frequency power during movement (compared to rest) in specific areas (Miller et al., 2020).

3.2.3 Recording brain activity

Neural circuits of interest can occupy brain territories of different shapes and sizes. Both too small and too big circuits are problematic to detect. Small circuits require high spatial resolution, and big circuits are detected only if a large enough brain area is covered. In response to that, different recording techniques were developed to decode activity in different brain areas.

There are many methods to directly or indirectly measure brain activity. First of all, some of them are invasive and some are not (see examples in Fig. 3.5). Another classification is based on what signal is measured. Direct methods, such as EEG, magnetoencephalography (MEG), ECoG, and deep electrodes record the electromagnetic activity of a brain, while indirect methods, such as functional Magnetic Resonance Imaging (fMRI) and positron emission tomography (PET), are based on oxygen, blood flow, or metabolic processes detection in brain areas, which are thought to be connected to neuronal activity. Additionally, some techniques, such as MEG, fMRI and PET, are too bulky or dangerous to use in everyday sleep. EEG and ECoG are the main potential tools for dream research, as they are direct and relatively comfortable.

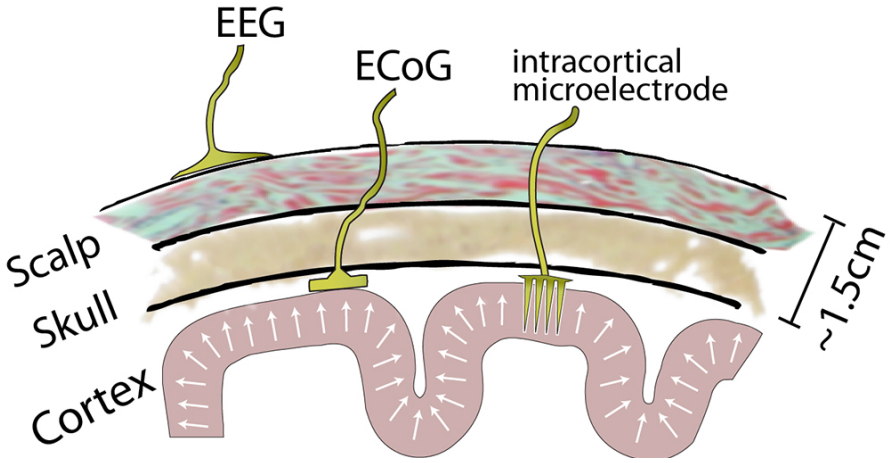

Figure 3.5: Electrode types used for BCIs: EEG is non-invasive, while ECoG and intra-cortical electrodes are invasive. Source: Miller et al. (2020).

EEG is a non-invasive and therefore safe recording procedure, although having a quite low spatial resolution compared to other recording technology, and being highly prone to artifacts. In EEG, electrodes are placed on the subject's scalp, which complicates maintaining low electrode impedance. As a person moves in bed through the night, it can be complicated to properly fix electrodes in place and get a consistent noise-free signal. Still, it is the most common way to record brain electromagnetic activity during sleep and is included in standard polysomnography, as it is mobile and easy to install (Leske & Dalal, 2019).

On the other hand, ECoG is a method of recording brain electrical activity by placing electrodes directly on the exposed cerebral cortex. It is an invasive technique which achieves better signal-to-noise ratio, temporal resolution and spatial resolution compared to non-invasive techniques like EEG, fMRI, or MEG (Cheng et al., 2019; Haufe et al., 2018; Leuthardt et al., 2021). One standard ECoG electrode with 5 mm surface area reads a group of about 500 000 neurons (Miller et al., 2020). The resolution can be higher using more dense electrode grids (Blakely et al., 2008; Kaiju et al., 2017). Leuthardt et al. (2021) classify ECoG as an intracranial method in terms of that a surgical procedure

is needed to implant the electrodes, which enter the intracranial space. Intracranial procedures have possibly life-threatening risks, such as brain infection and hemorrhage. Still, ECoG does not penetrate the brain tissue, and is safer compared to depth electrodes (Miller et al., 2020).

Despite a rising attention to the ECoG technology, there is still a lack of systematization and optimization for ECoG data processing methods, as this data remains to be relatively rare due to ethical limitations (Chiong et al., 2018; Miller et al., 2020; Pascarella et al., 2016). Consequently, ECoG and other invasive methods are used for functional mapping and surgery assessment only for patients with serious conditions, such as epilepsy and brain tumors, with little exceptions (Lai et al., 2020; RaviPrakash et al., 2020). It is also used in BCIs for patients with various functional limitations (Miller et al., 2020).

3.3 Working with brain data

3.3.1 Neural data processing

Raw ECoG data contains brain electromagnetic activity in temporal space. It has two dimensions: time and voltage fluctuations resulting from neuron ionic current. It is common to transform such data into spectral space, as it was shown that different frequency ranges have different power during different tasks (Miller et al., 2010; Sato et al., 2021). In spectral space, power (amplitudes) of specific frequency waves are obtained, while time dimension can be lost, e.g. after Fast Fourier Transform (FFT); or stay in the data, e.g. after Continuous Wavelet Transform (CWT). Lu et al. (2017) show that indeed spectral space is a better predictor than temporal space. They also argue that in the case of motor imagery classification, temporal localization of a spectral component contains less information than the frequency itself, making FFT better suited for this task than CWT.

An important additional dimension can be electrode locations. As it is common to record data using many electrodes at once, a more precise location of the signal can be found. It is important to note that while EEG has several widely used standards of electrode placements, ECoG placement varies from patient to patient depending on the area of interest (e.g. overlapping with a seizure focus). This makes ECoG data tough to work with when comparing several subjects.

Brain recordings often contain noise. A common source of noise is the power line interference. It contaminates a fixed frequency of 50 or 60 Hz depending on the country where the recording process took place. A spectrum of such contaminated data shows high narrow spikes for one of these frequencies (sometimes both) and its harmonics. The best way to avoid such noise is to record data in a shielded environment, but it is not always feasible, especially in home conditions. As a result, this noise should be removed before data analysis (e.g. with a notch filter).

Additionally, some recordings are affected by muscular or ocular activity, although its impact is less significant in ECoG data. Kovach et al. (2011) show that such noise can still contaminate intracranial data, especially by gamma bands from saccadic eye movements. The authors note that although this contamination is not always present, it should not be discounted.

3.3.2 Deep learning and Artificial Neural Networks

Artificial Neural Networks (ANNs) are a type of ML models which can automatically extract data features useful for predictions. Such networks are made of consecutive layers, each layer consists of nodes, called artificial neurons because ANNs are inspired by biological neural networks; moreover, it was found that they also train in a similar way to human brains (Caucheteux & King, 2022). Layers are connected similarly to synapses in the brain, as these connections have weights that control the strength of a signal transmitted between nodes. The number of nodes, connections, and layers can be fully customized to better fit a certain task. The goal of the ANN model is to minimize the objective

function, which is the function for mapping initial data into final predictions: labels in classification problems, or continuous values in regression problems. The more layers there are, the deeper is the network, which makes it more powerful in extracting useful data, as the objective function gets more parameters and can fit better. Moreover, each layer can perform additional data transformations on their inputs, and their output is further transformed by activation functions.

There are two main types of supervised learning models: classification and regression. Classification models return class probabilities from an input, while regression models return continuous values. They need different loss functions: classification models use functions such as Cross-Entropy, which reach higher probabilities for correct classes while lowering incorrect ones. Regression models use functions like mean squared error (MSE) or Mean Absolute Error, which reaches for smaller differences between the true and predicted values. ANNs are usually fit for classification problems, but they can be converted into regression models by changing the size and activation function of the last layer, and choosing the correct loss function.

ANNs and their variants show especially great potential to solve complex problems and analyze big data. They are often used for biological data and gain popularity in processing brain data. For example, Moses et al. (2021) used custom deep learning models to decode words directly from the cortical activity of a paralyzed person with 47.1 % accuracy; Shen et al. (2019) decoded images from fMRI recordings; and Sun et al. (2020) developed a deep learning architecture called Brain2Char, which can decode text directly from brain ECoG recordings, with 7 - 11 % error rate for vocabularies of 1200 - 1900 words.

CNNs show especially good results on image data sets (He et al., 2015), where feature location is important. CNNs apply convolution operations and efficiently simplify images into their smaller representations while retaining location information. CNNs are critically important in computer vision tasks, where they greatly reduce the number of features. There are many studies on CNNs for classifying brain tumors (e.g. Bhandari et al., 2020, and Deshpande et al., 2021). Location information is also available from electrode positions used to record data and can be used as a feature. For instance, Choi et al. (2018) used CNN to classify unimanual and bimanual movements from ECoG data recorded from a rhesus monkey. Another study was done by Meng and Xiang (2018), however, they first created a graph representation of a brain network using MEG electrodes as nodes, then transformed graphs into images and used these images for migraine detection with CNNs.

METHODS

4.1 Data

Two data sets were used for this work: motor imagery data was used for the model training and testing, and the REM sleep stage data was used for predicting only.

4.1.1 Motor imagery data

This data set was obtained from Miller (2016). The library contains ECoG data collected from several experiments. The experiment of interest was published by Miller et al. (2010) and contains recordings of 7 patients, two data files each: one is with a recording made during motor tasks, and another during motor imagery. Data is labeled with time points when there was a cue to do or imagine a specific movement. The movements were either simple and repetitive flexion and extension of all hand fingers, or opening a mouth with protrusion and retraction of the tongue. Cues were visual, with a written word indicating the body part to move, and lasted 3 seconds, with rest intervals (blank screen) in between. Full recordings have slightly different lengths for different patients, ranging from 376.6 to 390.9 s, the difference coming solely from the varying length of rest intervals.

Some contaminated channels were removed beforehand. The data was sampled at 1000 Hz and filtered by a bandpass filter from 0.15 to 200 Hz. Data is scaled in such a way that 1 amplifier unit equals 0.0298 μV.

Patients had a varying number of electrodes placed in different locations. The summary for each patient is provided in Table 4.1 and Appendix A.1. Electrode locations were presented in Talairach coordinates.

Patients FP and JM had some electrodes located outside of the standardized brain (see Figure 4.1), so they were dropped in this work.

Table 4.1: Number of channels for each subject from motor data. Note that BP data initially had 2 electrodes fewer from the full grid.

Patient	N channels	N badly mapped	Hemisphere
BP	6 x 8 - 2	0	Left
FP	8 x 8	4	Left
HH	6 x 8	0	Right
JC	6 x 8	0	Left
JM	8 x 8	8	Left
RH	8 x 8	0	Right
RR	8 x 8	0	Right

4.1.2 REM sleep data

The second data set was obtained from MNI Open iEEG Atlas, which is available at https://mni-open-ieegatlas.research.mcgill.ca. The data was described by von Ellenrieder et al. (2020). The Atlas contains readings from different types of electrodes, so data was selected and downloaded for subjects with subdural grids or strips placed over either frontal or parietal cortices, with 10 electrodes

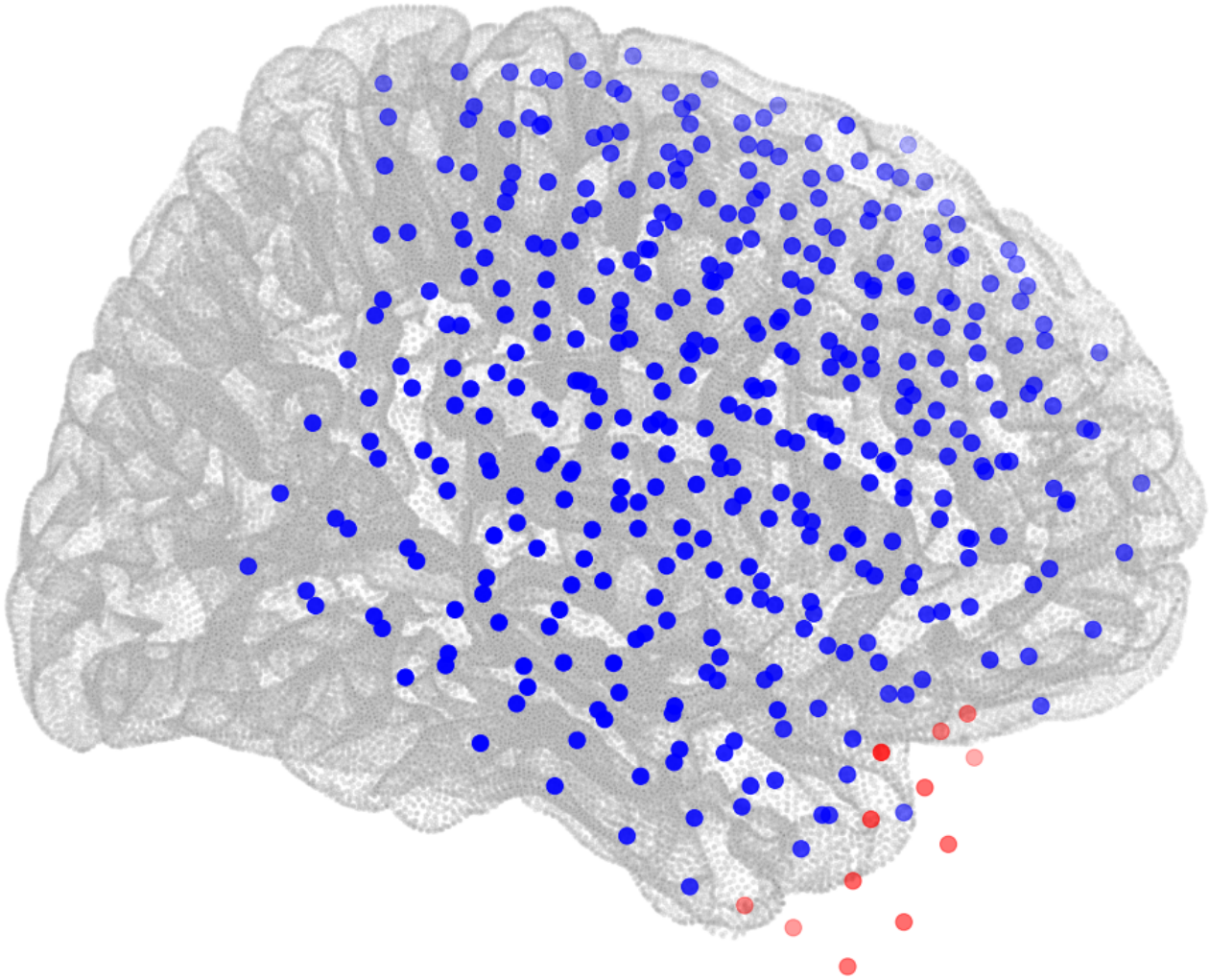

Figure 4.1: Electrode locations for all patients (mirrored to right hemisphere). Red dots indicate electrodes which are visibly "floating" as they were badly mapped to the standardized brain.

minimum. 6 subjects were collected this way (see Table 4.2). Their electrode locations were in MNI space, and were recalculated into Talairach space using this MNI-to-Talairach transform (Lancaster et al., 2007):

$$\mathrm{MTT} = \begin{bmatrix} 0.9357 & 0.0029 & -0.0072 & -1.0423 \\ -0.0065 & 0.9395 & -0.0726 & -1.3940 \\ 0.0103 & 0.0752 & 0.8967 & 3.6475 \\ 0 & 0 & 0 & 1 \end{bmatrix} \tag{4.1}$$

Coordinates of each electrode were multiplied with the MTT matrix. The resulting electrode locations are plotted in Figure 4.2.

The data is sampled at 200 Hz. It contains only channels which do not have epileptic activity recorded. Only the first 60 s of data was used, as after the 60th second, the signal is flat.

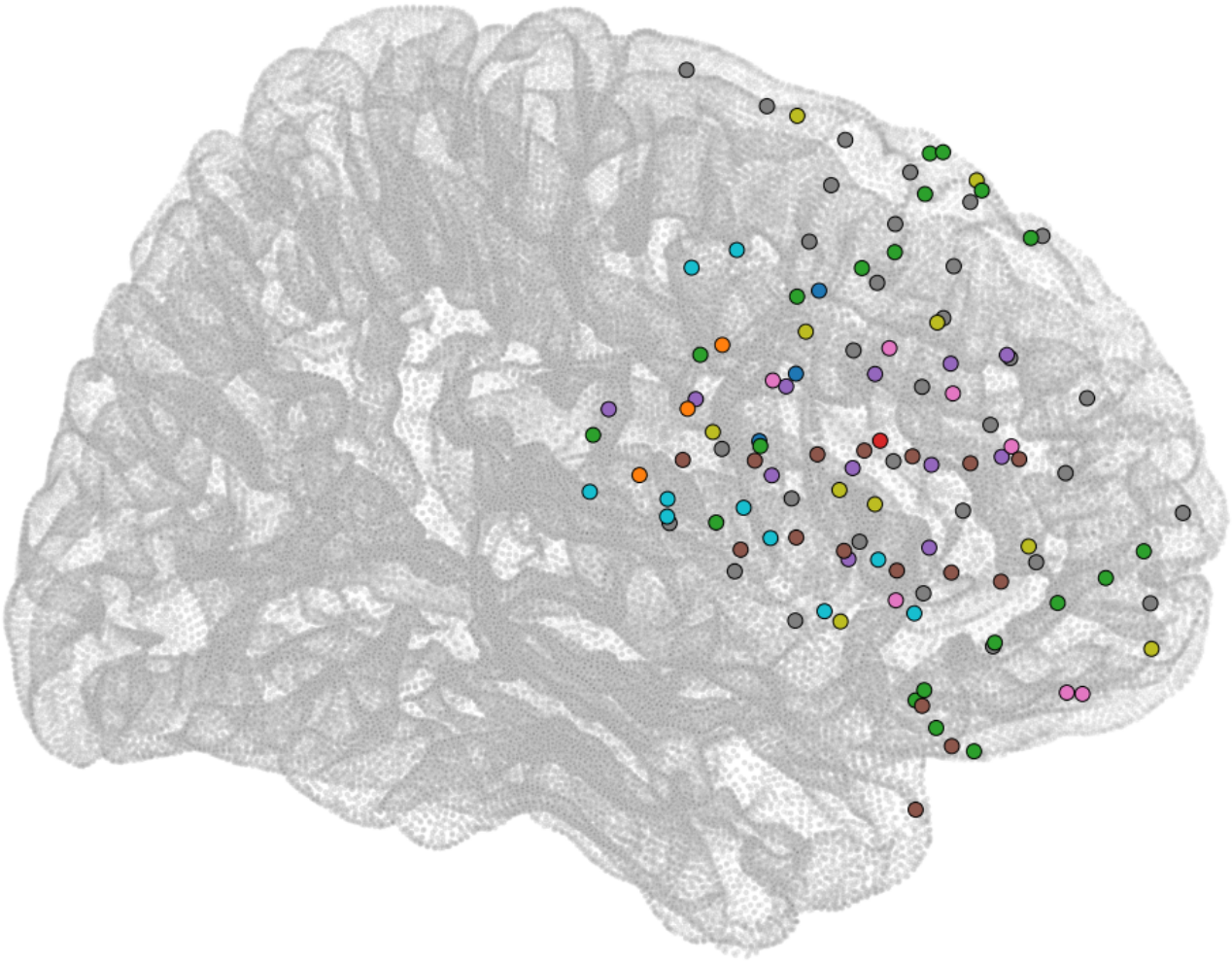

Figure 4.2: Electrode locations for all patients in REM sleep data (mirrored to right hemisphere). Different point colors correspond to different patients.

4.2 Data processing

4.2.1 Noise filtering

Miller et al. (2010) show that there is a significant change in power for 8 - 32 Hz and 76 - 100 Hz bands between task and rest. In this work, only these frequencies were used for training.

Motor data contained powerline noise in 60, 120, and 180 Hz bands. However, it was unnecessary to remove, because these frequencies are outside the range of interest. In REM sleep data, no powerline noise was already removed.

Data was filtered using Common Average Reference (CAR) mean filter as in Y. Liu et al. (2015). The signal s_h for each channel h for total H channels was calculated by this formula:

$$s'_h = s_h - \frac{1}{H} \sum_{i=1}^{H} s_i \cdot s_h \tag{4.2}$$

Table 4.2: Number of selected channels for each subject from REM sleep data.

Subject	N channels	Hemisphere
94	20	Both
99	12	Right
100	17	Right
103	31	Left
106	13	Both
110	10	Right

4.2.2 Activation visualization

To evaluate differences between brain activation from motor imagery and motor action tasks, extrapolated activation maps were plotted using the same steps as in Miller et al. (2010). That is, the data was filtered using CAR mean filter and fragmented by task cues. The first 500 ms were removed from each fragment, which resulted in 2500 ms fragments. Then, for each fragment, power spectral density (PSD) was calculated using the Welch method with 250 ms Hann window and 100 ms overlap. From calculated PSDs, 8 - 32 Hz and 76 - 100 Hz averaged broadbands were calculated, and the signed r-squared cross-correlation was calculated between PSDs of fragments with performing tasks and fragments of rest afterward, by the formula:

$$R = \frac{(PSD_{\text{task}} - PSD_{\text{rest}})^3}{|PSD_{\text{task}} - PSD_{\text{rest}}| \cdot s^2_{PSD_{\text{task}} \cup PSD_{\text{rest}}}} \cdot \frac{N_{\text{task}} \cdot N_{\text{rest}}}{(N_{\text{task}} + N_{\text{rest}})^2} \tag{4.3}$$

Here, s^2 is sample variance, and N_{task} and N_{rest} are numbers of task and rest fragments, respectively. Note that because there was exactly one rest fragment after each task fragment, $N_{\text{task}} = N_{\text{rest}}$, and the second fraction in this formula can be simplified to $\frac{1}{4}$.

The activation map consisted of calculated cross-correlations. Two-sample T-test was calculated between PSD_{task} and consequent PSD_{rest} fragments to assess the significance of the difference between them. Using only electrodes with significant differences between task and rest states, the activation map was interpolated using spherical Gaussian kernels with a size of about 5 mm (50 points). The results are provided in Appendix A.2.

4.2.3 Overlap metric

The overlap metric between different activation maps was calculated as in Miller et al. (2010). That is, a sum of Hadamard product (element-wise multiplication) between two map activation values was calculated as a test metric. Distribution of test metrics for 10^6 random permutations of activation values was generated. P-value was calculated as the probability for a test metric achieved after permutation to be larger than the metric achieved without permutation. P-values less than 0.05 were chosen to indicate the significance of the overlap between activation maps. The overlap metric itself was the value of the test metric in z-score units from the mean of permutations distribution.

4.2.4 Pre-training feature extraction

These types of feature extraction were applied for different models:

1. For models learning from temporal data (time-only models), it was filtered using a Butterworth bandpass filter from 8 to 100 Hz, then a bandstop filter from 33 to 75 Hz.

2. For models learning from spectral power (power-only models), it was obtained using the Welch method for PSD calculation, and only 8 - 32 Hz and 76 - 100 Hz were left in the data.

3. For models learning in both temporal and spectral data (time-power models), it was transformed with CWT using Morlet wavelet, which is a sine wave transformed with the Gaussian window (Russell & Han, 2016).

4.2.5 Spatial rearrangement

Several steps were done to add a more accurate signal location to the training data:

1. Electrode positions from all patients were loaded and joined into one group.
2. Electrodes on the left hemisphere were mirrored to the right hemisphere.
3. One dimension was removed with Principal Component Analysis (PCA), leaving each electrode with two new coordinates a and b instead of the initial three. PCA is a method to reduce the dimensionality of data by finding and keeping only principal components with the most explained variance.
4. Resulting coordinates were divided by the same number δ and rounded to whole numbers. δ was chosen by measuring the error between non-rounded and rounded coordinates, to sustain the balance between keeping both the error and data shape as small as possible.
5. Now, each electrode is represented by a specific cell in a $A \times B$ grid, where A and B are times of distance δ between the furthest electrodes in dimensions a and b, respectively. Different patients have different cells filled with data values. Unfilled values were left with zeros.
6. After channel signal transformation, each channel became a 2D array instead of 1D. Inserting these arrays into corresponding cells in the $A \times B$ grid resulted in 4D data samples of size $T \times A \times B \times F$.
7. Gaussian blur (see Eq. 4.4) was applied on the resulting samples along A and B dimensions. This filled empty cells with new values calculated from neighboring cells. Before applying blur, data was padded with zeros, so all cells with data had the same number of neighbor cells.

A Gaussian function is used to "smooth" the data. It's formula is:

$$G(x) = \frac{1}{\sqrt{2\pi\sigma^2}} e^{(} - \frac{x^2}{2\sigma^2}) \tag{4.4}$$

Here, σ is the standard deviation of the Gaussian distribution. For Gaussian blur, a kernel is applied to each data value to calculate a weighted average of the value's neighborhood.

To check whether spatial dimensions provide useful information, electrode positions are permuted for each patient. This results in the same shape of data, but spatial information becomes meaningless.

4.3 ANN model architecture

4.3.1 Linear layers

The simplest ANN layers are called Linear layers. A node from a linear layer takes a weighted sum of all its inputs, and like other layer types, passes it through an activation function. Its results can be described in a formula:

$$z = f(b + x \cdot \theta) = f(\sum_{i=1}^{n} x_i \theta_i) \tag{4.5}$$

Here, the vector of weights θ is the trainable part of the network, meaning that these numbers will change after each training epoch; it is also called a kernel, or sometimes a filter. b is the bias term, which is analogous to a constant in a linear function and allows the activation function to shift left or right. x is the data vector passed through the layer, n is the number of inputs into the node, and f is the activation function.

4.3.2 CNN layers

A CNN layer applies a convolution operation on a feature grid. The most common convolution type in computer vision is 2D convolution:

$$z = f(b + \sum_{k=1}^{C} x_i \star \theta_i) \tag{4.6}$$

Here, $\star$ is the 2D cross-correlation operator. C is the number of layer input channels.

A CNN layer can also apply a convolution operation on other dimensions, for instance, 1D or 3D. The $\star$ operation in the function will mean the cross-correlation operator of respective dimension.

Three more terms are important for CNN layers: padding, stride, and pooling. Padding is a technique of adding additional inputs located at the borders of the x sample when it is processed by a kernel. Usually, the values for these inputs are zeros. This can be done to retain the shape of x after the kernel operation because, without padding, the shape of x will shrink. Moreover, without padding, inputs close to borders are never multiplied with the center of a kernel.

Stride is a distance between the previous and the next kernel operation, which is analogous to the step of a rolling operation.

Pooling is another type of ANN layer, which is useful for further feature downsampling. Pooling kernel takes n neighboring inputs and calculates a single value using some simple function, like averaging or getting the maximum value. Pooling layers usually do not have weights and do not train.

4.3.3 Activation functions

As the result from an ANN layer is a multiplication between inputs and layer weights, output values can increase or vanish to zero quite fast. Activation functions transform the output so its values stay in a fixed range (e.g. from 0 to 1). Furthermore, activation functions are a source of nonlinearity which helps ANNs to better fit to data.

Usually, activation functions are applied after each layer. Most common ones in simpler ANN and CNN architectures are Sigmoid (i.e. Logistic) (4.7), Hyperbolic Tangent (4.8) and Rectified Linear Unit (ReLU) (4.9) functions:

$$F_{\text{Sigmoid}} = \frac{1}{1 + e^{-x}} \tag{4.7}$$

$$F_{\text{Tanh}} = \frac{e^{x} - e^{-x}}{e^{x} + e^{-x}} \tag{4.8}$$

$$F_{\text{ReLU}} = \max(0, x) \tag{4.9}$$

The ReLU function is currently popular in deep neural networks as it is much faster to calculate (He et al., 2015). It is also capable of outputting a true zero value, which results in sparse layers; this will additionally accelerate and simplify the model. Moreover, it reduces the likelihood of a problem called the vanishing gradients, when model weights change is very small or non-existent, which stops the training of the model. The vanishing gradient problem is inherent in the Sigmoid function, as its

derivative is always less than 1, and a product of several Sigmoid functions quickly decreases to zero. ReLU makes the gradient change constant, which results in faster learning.

On the other hand, ReLU can result in the inverse problem called the exploding gradients. This happens because large gradients accumulate and make the model unstable and incapable of training. Two possible solutions for this problem are clipping the gradient value to not allow it to pass a certain threshold, and decreasing the number of layers in the model.

4.3.4 Loss function

A loss function compares the final result from the network output with the ground truth. Different loss functions are used for different tasks. The Cross-Entropy loss is common for classification tasks:

$$L_{\text{CE}} = -\sum_{m=1}^{M} w_m y_{o,m} \ln(p_{o,m}) \tag{4.10}$$

Here, M is the number of classes; y and p are the binary indicator and the predicted probability that observation o is of class m, respectively. w_m is the weight for class m, and providing different weights for classes is helpful when data is imbalanced (some classes are over-represented while others are under-represented). L_{CE} is the loss calculated for one data sample, while the final loss value for all data is the average of all individual loss values. The Cross-Entropy function is also suited for multi-class problems, where several classes can be assigned to one sample.

4.3.5 Optimizers

Similra to other machine learning algorithms, ANN models can learn data features because of back-propagation. Backpropagation computes the gradient of the loss function with respect to the weights of the network. To reach a minimum (i.e. reduce the loss), model weights are changed by an optimization algorithm, called optimizer. The most basic optimizer is Gradient Descent (Ruder, 2017):

$$\theta_{t+1} = \theta_t - \alpha \cdot \nabla J(\theta_t) \tag{4.11}$$

Here, α is the learning rate – the small step the function makes towards the minima. $\nabla J(\theta)$ shows the direction of the fastest increase for function J, which is the objective function.

Gradient Descent is relatively easy to compute and understand, but it calculates the gradient on the whole data set, which makes it slow. Moreover, it may stop at local minima with unacceptable accuracy or low generalization level. A version of Gradient Descent, called Stochastic Gradient Descent (SGD), tries to update model weights more frequently, which makes it faster and requires less memory. On the other hand, it is more difficult to stabilize even at low enough minima, so the learning rate needs to be gradually reduced while training progresses. SGD has the same formula as Gradient Descent, but it updates θ weights after each data sample, not the whole data set.

Other optimizers were developed for deep learning networks, one of the most popular being Adam. It stores an exponentially decaying average of past gradients m_t and squared gradients v_t and computes their corrected versions $\hat{m}_t$ and $\hat{v}_t$:

$$m_t = \beta_1 m_{t-1} + (1 - \beta_1) g_t \tag{4.12}$$

$$v_t = \beta_2 v_{t-1} + (1 - \beta_2) g_t^2 \tag{4.13}$$

$$\hat{m}_t = \frac{m_t}{1 - \beta_1^t} \tag{4.14}$$

$$\hat{v}_t = \frac{v_t}{1 - \beta_2^t} \tag{4.15}$$

$$\theta_{t+1} = \theta_t - \frac{\mu}{\sqrt{\hat{v}_t} + \epsilon} \hat{m}_t \tag{4.16}$$

μ is a learning rate that is no more a constant like α but is changed for each weight and each t step. Common hyper-parameter values for Adam are: $1e-8$ for ϵ, which is a smoothing term to avoid division by zero; 0.9 for β_1, and 0.999 for β_2 (Ruder, 2017).

4.3.6 Regularization methods

The Adam optimizer boosts the speed of learning considerably but introduces an additional chance for the model to overfit, which means it memorized the training data but failed to extract generalized features and thus shows high errors for test data. Various methods to reduce the chance of overfitting are called regularization.

The simplest technique to reduce the chance of overfitting for ANNs is called Dropout, which replaces random values of the input tensor with zeros with a certain probability, which is often set to 50 %. Another popular regularization method is batch normalization. It is normalization done between the ANN layers along mini-batches. Without normalizing the data, the model can inflate the importance of values that are substantially higher than others. Batch normalization also helps against exploding gradients.

4.4 Model scoring

Multi-class confusion matrices can be calculated to estimate trained model accuracy. A confusion matrix has the size of $M \times M$ (M is the number of classes) and contains values that show how many predictions for each class were received from the model for each actual class. A basic example for three classes is visualized in Table 4.3, where green-colored cells should contain correct prediction counts, and red-colored cells should contain counts for incorrectly predicted samples.

Table 4.3: A basic scheme for multi-class confusion matrix with 3 classes.

		predicted			total
		0	1	2	true
true	0				
	1				
	2				
total predicted					

For each class, the correct predictions are called True Positives (TP). Incorrectly labeled samples of class m are False Negatives (FN). Samples of other classes labeled as m are False Positives (FP). Lastly, all other samples which are not m and are not labeled as m are True Negatives (TN).

From the confusion matrix, accuracy, precision, recall, and F1 scores are calculated for each class using these formulas:

$$F_{\text{Accuracy}} = \frac{\text{TP} + \text{TN}}{N} \tag{4.17}$$

$$F_{\text{Precision}} = \frac{\text{TP}}{\text{TP} + \text{FP}} \tag{4.18}$$

$$F_{\text{Recall}} = \frac{\text{TP}}{\text{TP} + \text{FN}} \tag{4.19}$$

$$F_{\text{F1}} = 2\frac{F_{\text{Precision}} \cdot F_{\text{Recall}}}{F_{\text{Precision}} + F_{\text{Recall}}} \tag{4.20}$$

Here, N is the total number of samples.

The resulting metrics can be compared with baselines, which are calculated by labeling every sample with the same class, which is the most abundant in the data set.

4.5 Data and software availability

The data is freely available to download. All codes were written using Python 3.8.8, which is a popular and freely available programming language. Additionally, Python packages were used:

- Numpy 1.20.3: main computations with N-dimensional arrays;
- Scipy 1.6.2: Matlab-formatted data reading, signal filters, and CWT;
- Sklearn 0.24.1: data scaling and transformations for ML;
- PyTorch 1.10.1: model design and implementation;
- Matplotlib 3.3.4: visualizations.

All listed packages are free and well documented. All codes are published in a Github repository and freely available by link: https://github.com/Tallivm/readream-motor.

4.6 Ethics statement

All patients participated in a purely voluntary manner, after providing informed written consent, under experimental protocols approved by the Institutional Review Board of the University of Washington (#12193). Portions of these data originally appeared in the manuscript "Cortical activity during motor execution, motor imagery, and imagery-based online feedback" published in Miller et al. (2010). Portions of these patient data were anonymized according to the IRB protocol, in accordance with HIPAA mandate. It was made available through the library described in "A Library of Human Electrocorticographic Data and Analyses" by Miller (2016), freely available at https://searchworks.stanford.edu/view/zk881ps0522

RESULTS

5.1 Data processing pipeline and model selection

Data processing pipeline is visualized in Figure 5.1. Data were filtered using CAR mean filter, zero averaged, and fragmented by cues. From each fragment, the first 500 s were removed, and the remaining data split into N fragments of length 200 s with 100 s overlap. After that, different steps were done depending on the model type. To speed up the training process, the resulting $T \times 25 \times 21 \times F$ samples were made into $\frac{T}{2} \times 25 \times 21 \times \frac{F}{2}$ by applying a mean rolling window along T and F axes.

Motor data was split into train and test parts with a 9-to-1 ratio, respectively. There were from 284 to 298 fragments in motor data for a single patient, and 118 fragments for each patient in REM sleep data.

In motor data, "rest" class is present about two times more frequently than other classes, so it was used to calculate baselines. The resulting baseline values are:

- Baseline accuracy: 51 %;
- Baseline precision: 51 % for "rest" class, 0 % for other classes, with 17 % macro average and 26 % weighted average;
- Baseline recall: 100 % for "rest" class, 0 % for other classes, with 33 % macro average and 51% weighted average;
- Baseline F1 score: 68 % for "rest" class, 0 % for other classes, with 23 % macro average and 34 % weighted average.

5.1.1 Model architectures

The model architecture was selected as shown in Figure 5.2. It contains two CNN layers and two linear layers. The first CNN layer transforms input along temporal axis, applies ReLU activation and pools maximum values along spatial A and B axes. The second CNN layer is composed of two separate kernels, one learns from low-frequency power, and the other from high-frequency power. Each kernel transforms half of the data along the spectral axis, applies ReLU activation, and pools maximum values along spatial A and B axes. After each CNN layer, Batch normalization and Dropout (with 50 % probability) are applied. The resulting data is flattened and is transformed with the linear layers to get M values (which is the number of classes), on which the Softmax activation function is applied to get class probabilities. Loss was calculated with Cross-Entropy loss function. CNN layer weights were initiated with He initialization, which has a normal distribution with $2/n$ variance (He et al., 2015).

Other model hyper-parameters were the same for each trained model:

- Class weights for the loss function: 1 for "rest", 2 for "hand", 2 for "tongue";
- Optimizer: Adam ($\epsilon = 1e-8$, $beta_0 = 0.9$, $beta_1 = 0.999$);
- Learning rate: $5 \cdot 10^{-4}$;
- Weight decay: $5 \cdot 10^{-6}$.

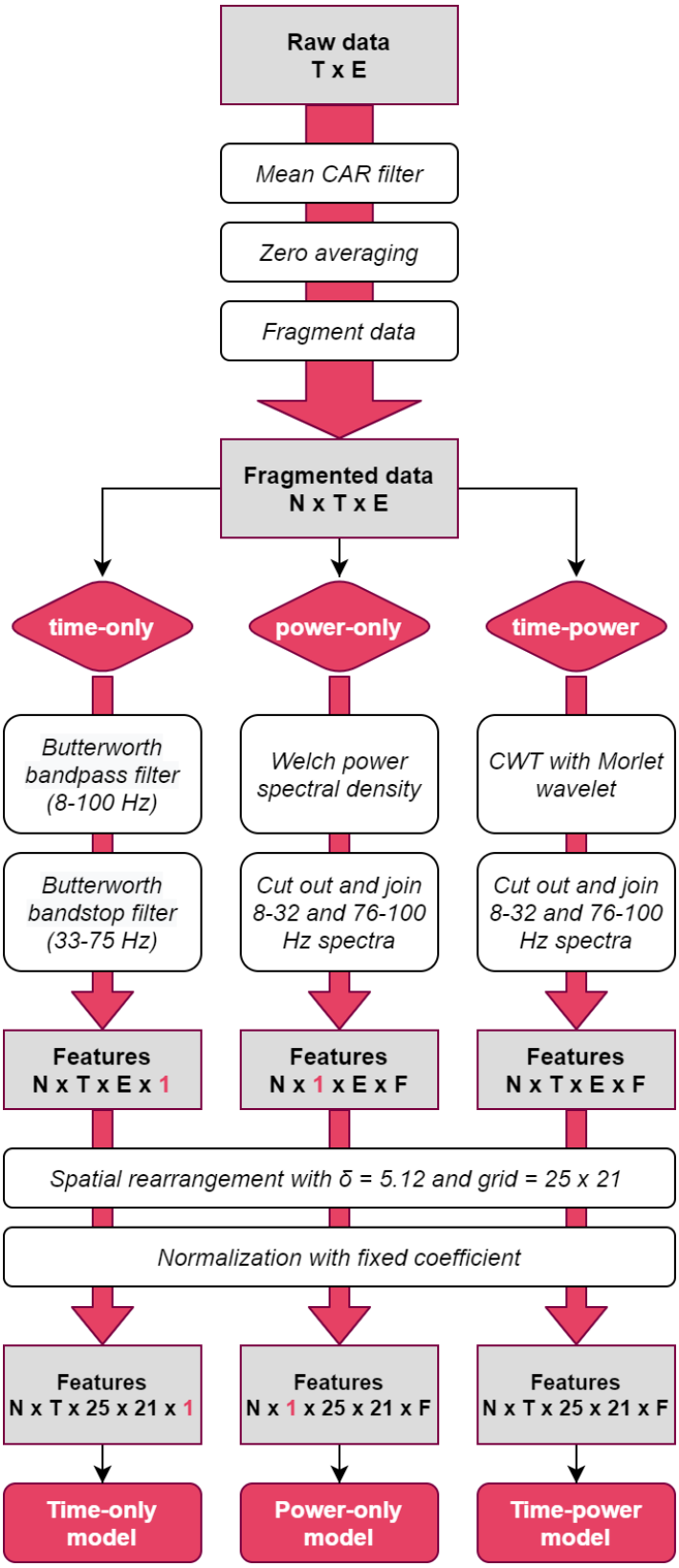

Figure 5.1: The pipeline for data processing used for different types of models: time-only models, power-only models, and time-power models.

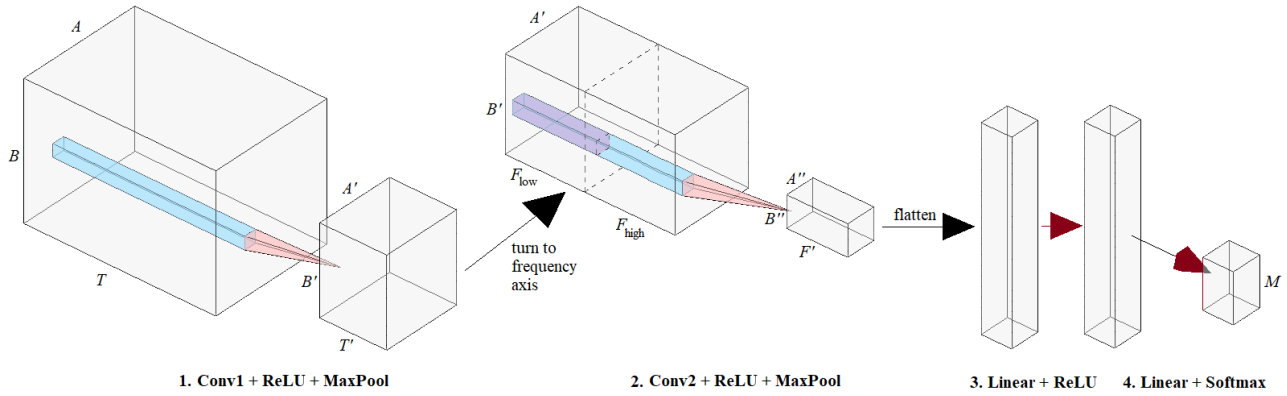

Figure 5.2: Time-power model architecture used for data with electrode location information. Grey cuboids represent data samples, which are 4-dimensional, but one dimension is not visible. CNN layers are visualized in red, and their kernels in blue or violet. T' and F' denote changed size of temporal and spectral axes, respectively. A' and A'' denote changed size of A axis one or two times, same for B' and B''.

5.1.2 Different model types based on training features

To estimate the difference between activation from hand and tongue tasks, overlap metrics between hand and tongue activation maps were calculated for either motor imagery or motor action data. The results are shown in Table 5.1.

Table 5.1: Overlap metrics between activation after hand or tongue clue for each patient, for either motor imagery or motor action experiments. Values are significant (p-value < 0.05), otherwise denoted by ø. MI: motor imagery; MA: motor action.

Patient	MI, 8-32 Hz	MA, 8-32 Hz	MI, 76-100 Hz	MA, 76-100 Hz
BP	ø	ø	ø	ø
FP	2.586	4.217	2.763	1.737
HH	3.499	4.994	ø	2.050
JC	1.959	2.630	ø	ø
JM	3.724	4.781	ø	3.547
RH	ø	ø	1.603	ø
RR	4.226	2.816	4.231	ø

Three model types were compared between each other: time-only, power-only, and time-power. In the chosen model, the first CNN layer learns from temporal information and the second one - from spectral information. Consequently, for time-only models, the second CNN layer was omitted, and the sample was flattened right after the first CNN layer. Similarly, for power-only models, the first CNN layer was omitted. The loss changes during the training are provided in Figures 5.3 for all three model types, and confusion matrices are visualized in Figure 5.4.

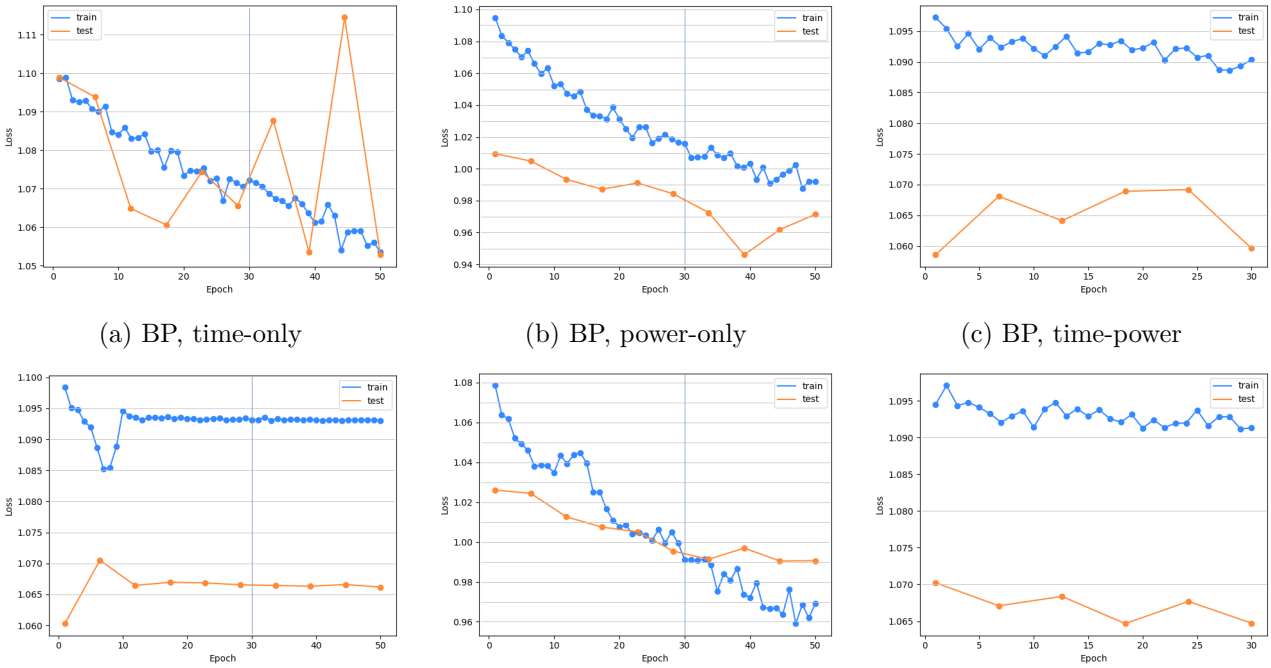

(a) BP, time-only (b) BP, power-only (c) BP, time-power

(d) RR, time-only (e) RR, power-only (f) RR, time-power

Figure 5.3: Loss change during training for time-only, power-only, and time-power models, trained on imagery data, for two patients separately: BP and RR. Note that time-power models were trained for 30 epochs instead of 50 epochs. For better comparison, time-only and power-only models have vertical lines on the 30-th epoch.

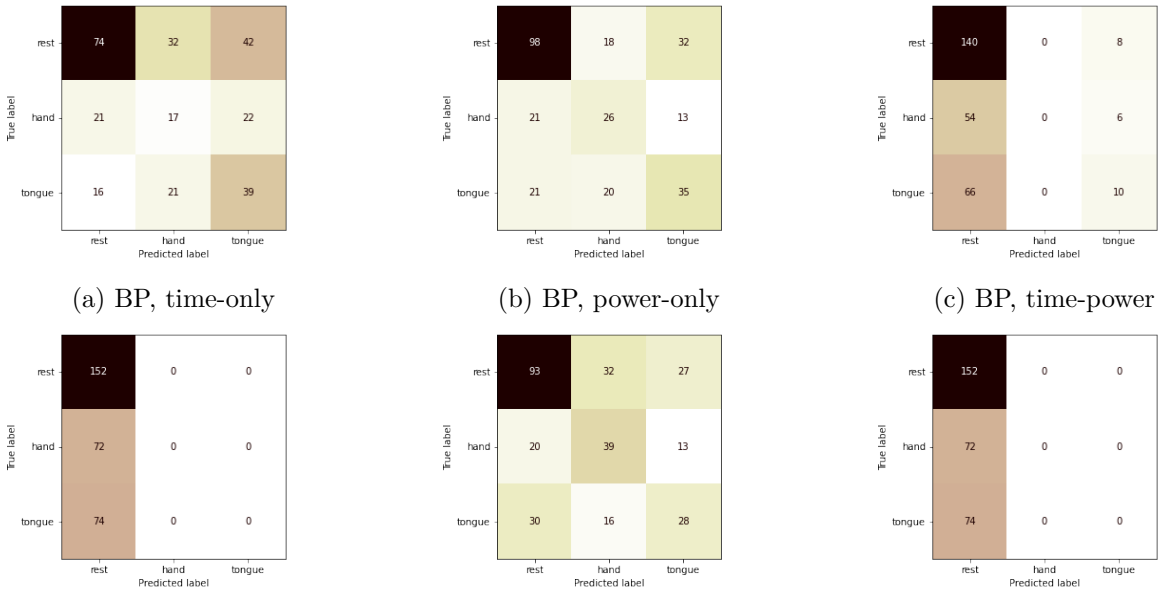

(a) BP, time-only (b) BP, power-only (c) BP, time-power

(d) RR, time-only (e) RR, power-only (f) RR, time-power

Figure 5.4: Confusion matrices for time-only, power-only, and time-power models, trained on motor imagery data. Note that time-power models were trained on 30 epochs instead of 50 epochs as for time-only and power-only. For testing, same data was used as for plotting test loss change, that is, from the same patient and motor category.

5.1.3 Choosing spatial rearrangement parameter

An example of adding simplified spatial information into data is shown in Figure 5.5. The δ parameter was chosen by calculating grid size and distance error ratio for different δ values between 1 and 10 while ensuring no electrode overlap for the same patient. Ratios are visualized in Figure 5.6. The maximum δ with which no electrodes overlap within the patient was 6.21, which reduced unique electrode locations by 45.85 %, and produced a grid of size 21×18, with a mean distance error of 39.31 % (SD = 14.36 %) from the minimum distance between electrodes in a single ECoG grid.

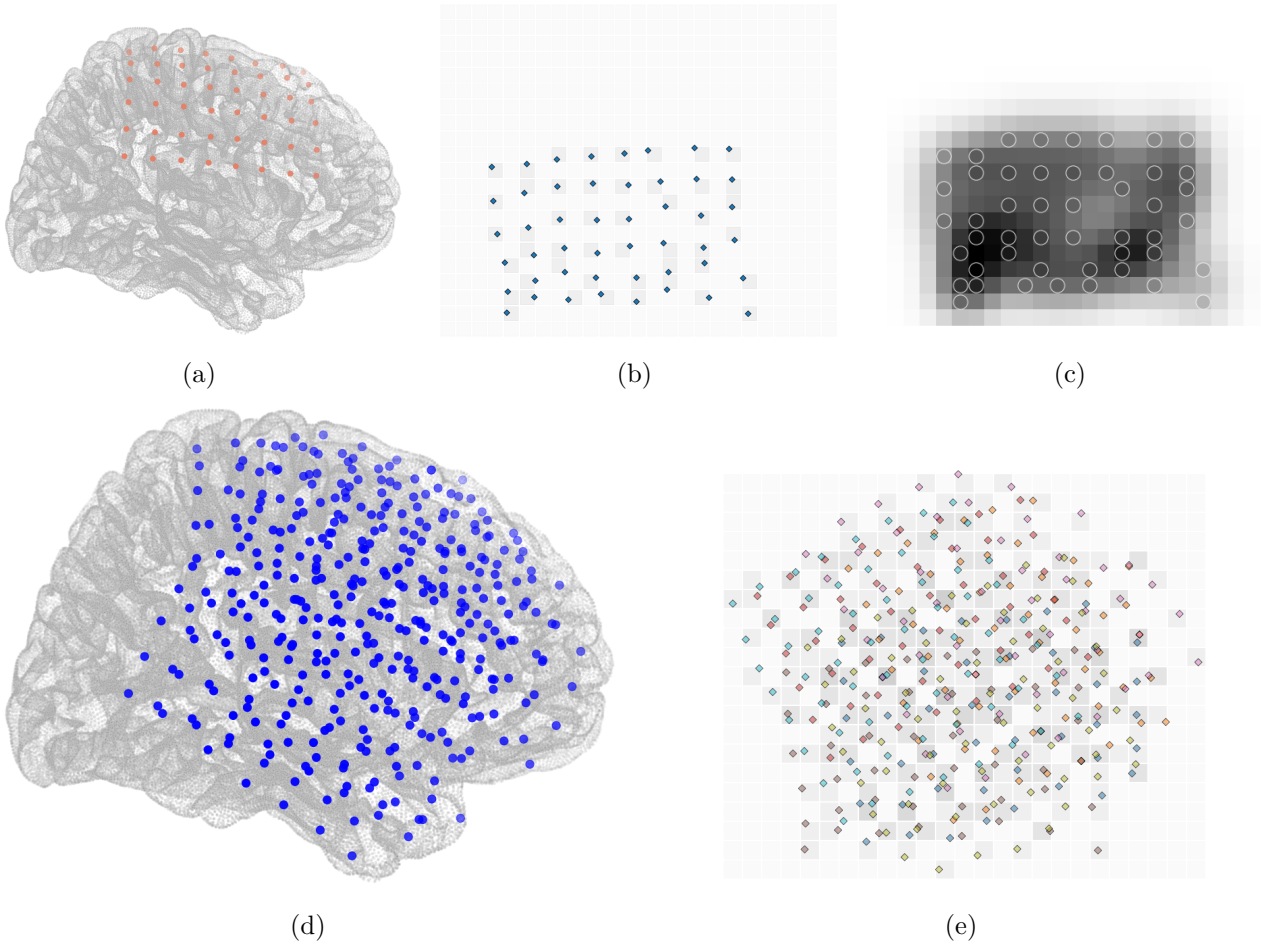

(a) (b) (c)

(d) (e)

Figure 5.5: A visualization of spatial transformation applied on the first patient in motor data. (a): initial electrode positions plotted on a standardized brain. (b): simplified electrode positions (blue), placed on a simplified $A \times B$ grid (generated from all patients). Darker grid cells overlap with at least one electrode (only one overlap per electrode is counted). (c): after temporal and spectral axes with data are added, Gaussian blur is applied on the resulting 4D tensor along A and B axes to fill empty grid cells with extrapolated data; the darkness of a cell is proportional to the number and proximity of surrounding electrodes. (d): initial electrode positions for all patients (mirrored to the right hemisphere) which were used to generate the simplified grid. (e): simplified electrode positions after the spatial transform.

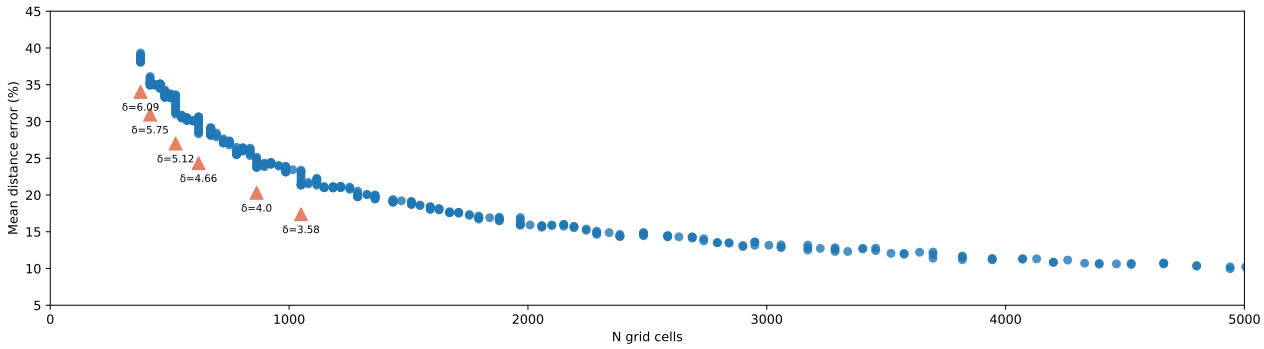

Figure 5.6: Ratio between grid size and mean distance error between old and new electrode locations. Some δ are noted by orange triangles.

To balance between grid size and error size, $\delta = 5.12$ was chosen. It resulted in a decrease of unique electrode locations by 34.97 %, with a grid size of 25×21, and a mean distance error of 31 % (SD=12.11 %) (from the minimum distance between electrodes in a single ECoG grid). The resulted grid with all electrodes plotted on it is visualized in Figure 5.5(e).

To evaluate whether spatial information is useful for models, two models were trained: the first model was trained on data with correct spatial information, and the second model - on data, where electrodes were randomly changed places. The loss changes are provided in Figure 5.7.

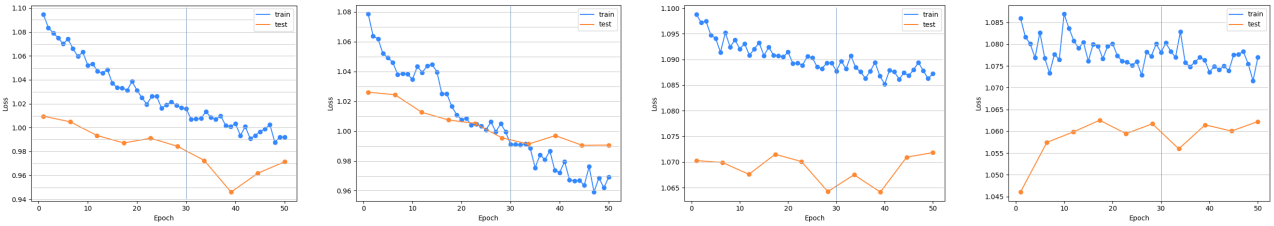

(a) BP, power-only, correct (b) RR, power-only, correct (c) BP, power-only, permuted (d) RR, power-only, permuted

Figure 5.7: The effect of electrode location permutation on model training speed. "correct" means no location permutation was performed.

5.2 One-patient models vs many-patients models

Overlap between patient grids was checked after the spatial transform. This was helpful to estimate the similarity between patient activation patterns using overlapping electrodes. A summary of electrode location overlap is provided in Table 5.2. Activation maps were compared for the same data and clue types between patients using only overlapping electrodes (see Fig. 5.8).

Table 5.2: Number of overlapping electrode positions between patients after mapping to a simplified grid.

	BP	FP	HH	JC	JM	RH	RR
BP	46	9	5	2	8	15	3
FP	9	60	4	5	19	6	20
HH	5	4	48	7	2	4	10
JC	2	5	7	48	3	13	6
JM	8	19	2	3	56	12	12
RH	15	6	4	13	12	64	6
RR	3	20	10	6	12	6	64

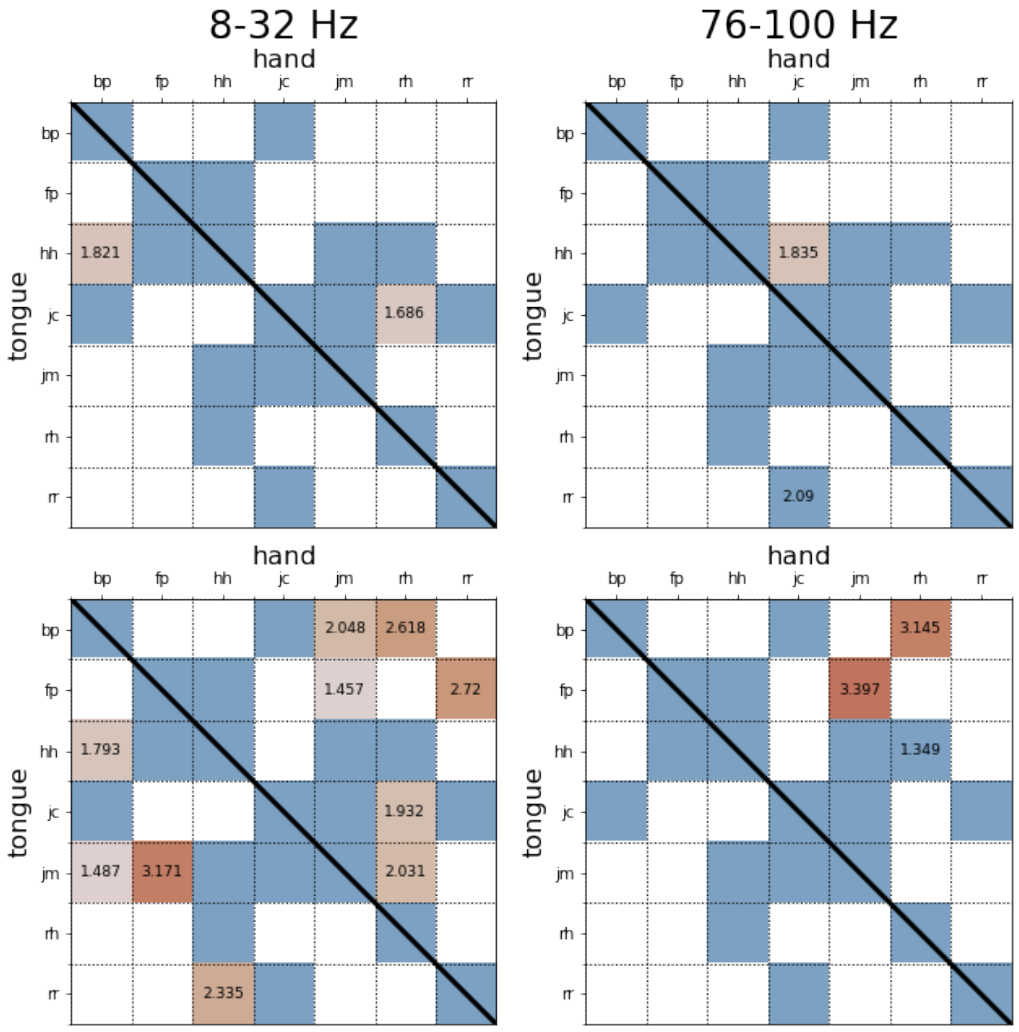

Figure 5.8: Overlap metrics for patient pairs in each task group. The top row corresponds to motor imagery data, bottom row – to motor action data. Top-right corners of matrices are for hand tasks, while the bottom-left corners are for tongue tasks. Only significant overlap metrics are provided. Brown color intensity corresponds to value. Irrelevant pairs are colored light blue: patients overlapping with themselves, as well as overlaps with less than 5 electrodes. White cells correspond to pairs for which the overlap is not significant (p-value > 0.05).

To check whether the overlap helps the model train, additional power-only models were trained on motor action data:

1. The first was trained on FP and RR patients' data, as they have the biggest number of overlapping electrodes (20) and their low band hand activation maps overlap.
2. The second model was trained on FP and JM patients' data, as it overlaps in both high and low-frequency power for hand movements, and has 19 overlapping electrodes.
3. The third model was trained on JM and RR patients' data. Although these two patients have 12 overlapping electrodes, they have no overlapping activity.

Loss changes are visualized in Figure 5.9.

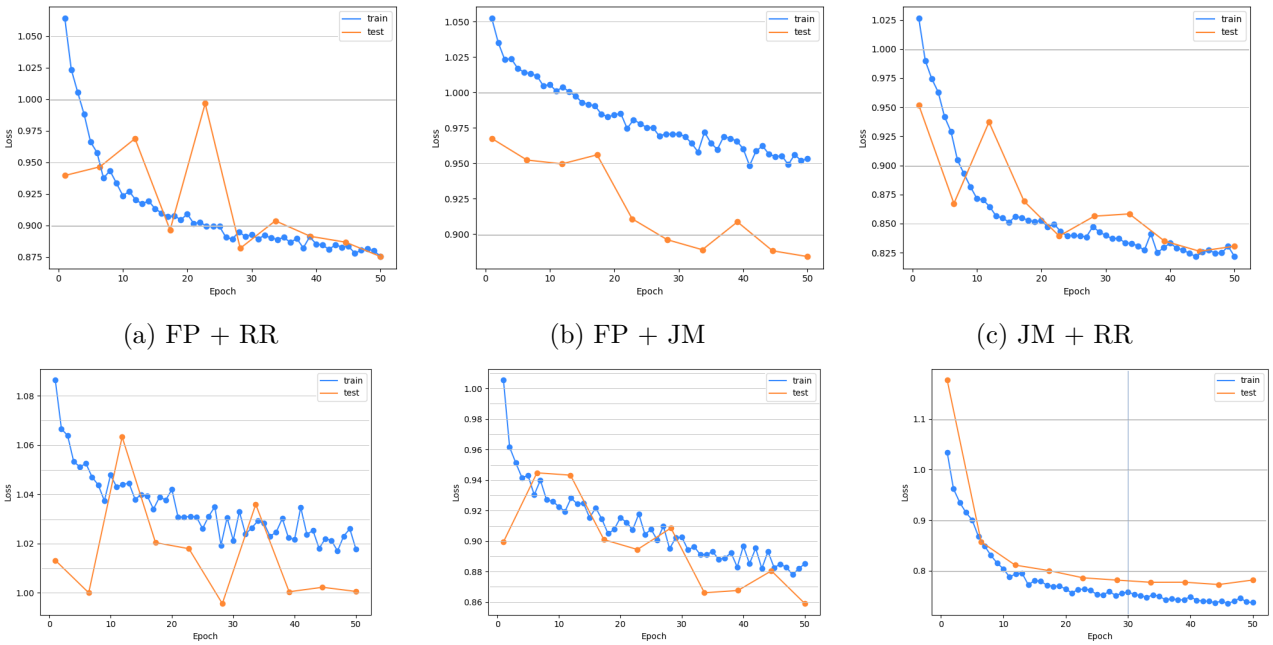

(a) FP + RR (b) FP + JM (c) JM + RR

(d) FP (e) JM (f) RR

Figure 5.9: A comparison between two-patient models (top row) and one-patient models (bottom row). All patients are power-only and trained on motor action data.

Additionally, all patients were cross-tested on both motor imagery and real motor data to evaluate the overlap between their features learned by models (see Fig. 5.10).

5.3 Imagery vs real motor data in training set

After calculating overlap significance between motor imagery and motor action activation maps, results were used to decide whether actual motor fragments can be added to the train set without introducing additional variance. The results are shown in Table 5.3.

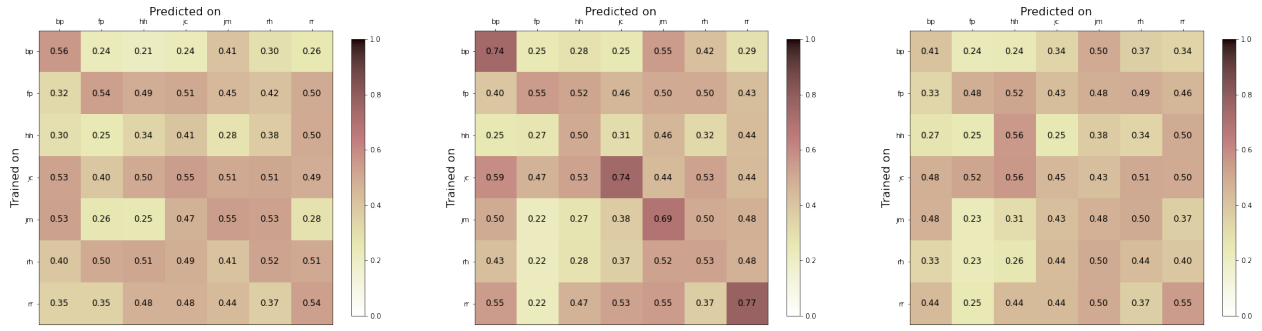

(a) Motor imagery data

(b) Motor action data

(c) Motor imagery from motor action data

Figure 5.10: Cross-test accuracy values for each patient pair. (a): motor imagery prediction accuracy using power-only models trained on motor imagery. (b): motor action prediction accuracy using power-only models trained on motor action. (c): motor imagery prediction accuracy using power-only models trained on motor action.

Table 5.3: Overlap metrics between motor imagery and motor action activation for each patient. Values are significant (p-value < 0.05), otherwise denoted by ø. H: hand, T: tongue.

Patient	H, 8-32 Hz	T, 8-32 Hz	H, 76-100 Hz	T, 76-100 Hz
BP	ø	ø	ø	ø
FP	5.428	4.355	4.261	5.423
HH	3.903	4.601	ø	3.864
JC	5.498	2.795	4.463	3.235
JM	5.854	3.815	4.078	2.231
RH	1.937	3.152	ø	3.213
RR	3.305	5.713	ø	ø

Additionally, models were trained on motor imagery, motor action only, or using both motor imagery and action, while testing only on imagery data. The model which was trained on both motor imagery and motor action had about two times bigger training set. The results are compared in Figure 5.11.

5.4 Predictions on REM sleep data

Before making predictions from REM sleep data, additional models were trained using a different data fragmentation approach, which simulates real-time prediction. That is, instead of fragmenting by task cues, data was fragmented by a window, so a cue can occur in any place of the fragment. As a result, fragments could consist of two classes at once. This Window-based model solved the multi-class classification problem by predicting the percentage of each class in the data sample. Power-only and time-only models were trained using window fragmentation. The results were compared with the respective models from cue fragmentation (see Fig. 5.12).

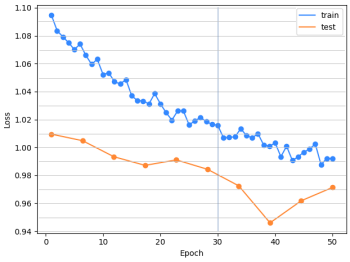

(a) BP, motor imagery

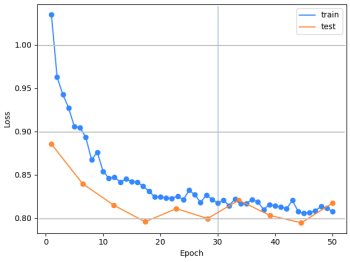

(b) BP, motor action

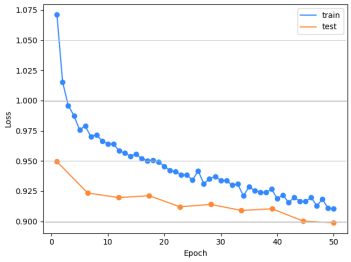

(c) BP, motor imagery + action

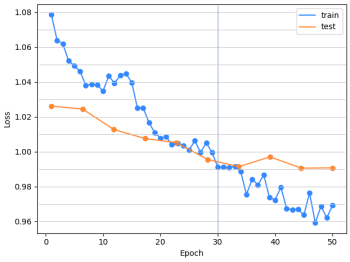

(d) RR, motor imagery

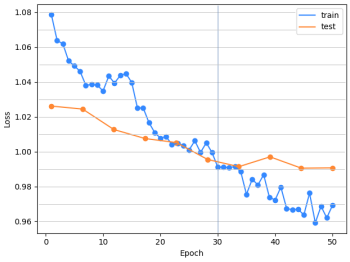

(e) RR, motor action

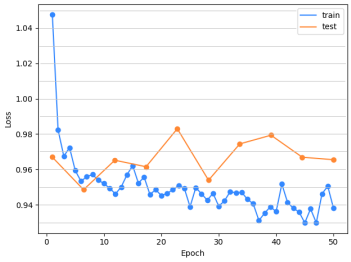

(f) RR, motor imagery+action

Figure 5.11: Loss change comparison between power-only models, trained either on motor imagery or motor action data.

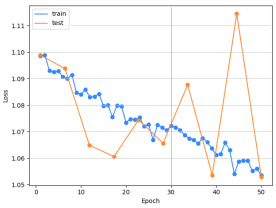

(a) BP, time-only, cues

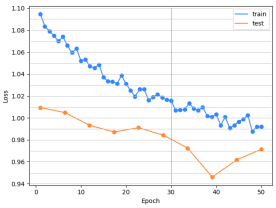

(b) BP, power-only, cues

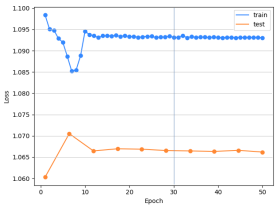

(c) RR, time-only, cues

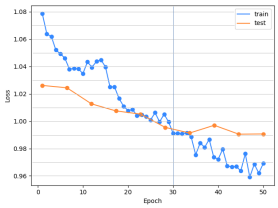

(d) RR, power-only, cues

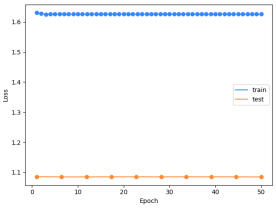

(e) BP, time-only, windows

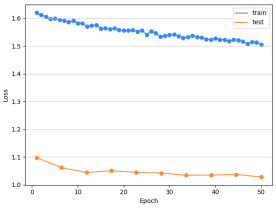

(f) BP, power-only, windows

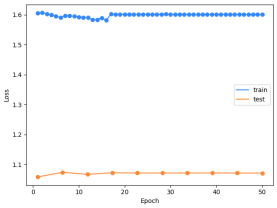

(g) RR, time-only, windows

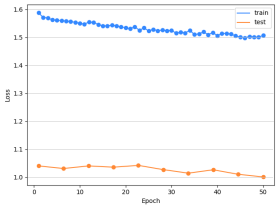

(h) RR, power-only, windows

Figure 5.12: Loss change comparison between models trained on differently fragmented motor imagery data.

It was impossible to calculate activation maps for REM sleep data the same way as for motor data, as REM sleep data contains no labels. To check the overall similarity of motor and REM sleep data, the spectral power was compared (shown in Fig. 5.13).

As the last step, the every one-patient model was used to find motor imagery in REM sleep data. The summary of predictions is shown in Table 5.4.

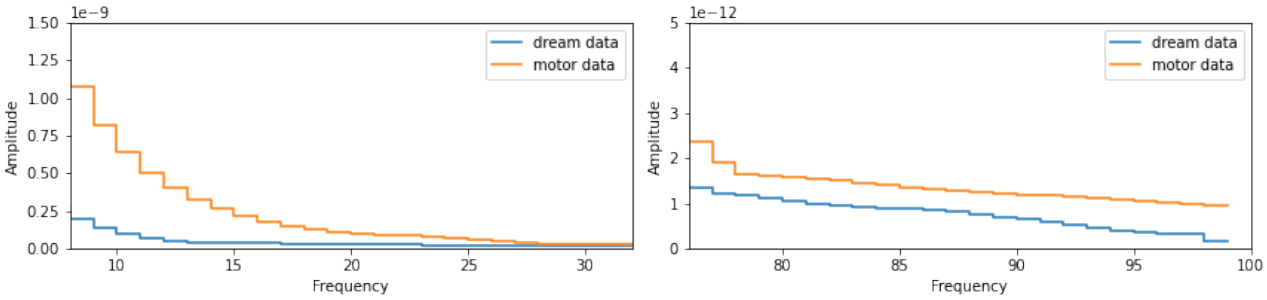

Figure 5.13: Comparison of Welch spectral power density in bands of interest (8 - 32 Hz and 76 - 100 Hz) between motor data and REM sleep data. Motor data shows higher power than REM sleep data overall.

Table 5.4: Results of motor imagery predictions on REM sleep data using power-only one-patient models trained on motor imagery. Columns denote models used, rows denote subjects from REM sleep data. Each cell contain three values - numbers of predictions of a class - with a format like this: "rest" | "hand" | "tongue".

	BP	FP	HH	JC	JM	RH	RR	Mean
94	0 | 93 | 25	118 | 0 | 0	81 | 35 | 2	89 | 0 | 29	118 | 0 | 0	118 | 0 | 0	116 | 1 | 1	91.4 | 18.4 | 8.1
99	83 | 29 | 6	118 | 0 | 0	110 | 8 | 0	72 | 17 | 29	118 | 0 | 0	49 | 0 | 69	118 | 0 | 0	95.4 | 7.7 | 14.9
100	66 | 52 | 0	118 | 0 | 0	118 | 0 | 0	44 | 72 | 2	118 | 0 | 0	0 | 0 | 118	41 | 77 | 0	72.1 | 28.7 | 17.1
103	1 | 0 | 117	118 | 0 | 0	118 | 0 | 0	54 | 53 | 11	118 | 0 | 0	118 | 0 | 0	117 | 1 | 0	92 | 7.7 | 18.3
106	16 | 19 | 83	2 | 116 | 0	43 | 75 | 0	114 | 0 | 4	118 | 0 | 0	118 | 0 | 0	114 | 4 | 0	75 | 30.6 | 24.9
110	110 | 0 | 8	0 | 118 | 0	118 | 0 | 0	38 | 10 | 70	118 | 0 | 0	113 | 0 | 5	116 | 2 | 0	87.6 | 18.6 | 11.9

DISCUSSION

6.1 The development of the pipeline

6.1.1 The motivation for spatial rearrangement

After comparing model effectiveness with permuted/correct electrode locations (see Fig. 5.7), it can be seen that spatial information helps lower the loss for both BP and RR patients. Permutation of electrode locations resulted in 3 - 4 times slower loss change for both patients, and the loss curve looks more unstable, especially for the RR patient. A conclusion can be drawn that CNN layers indeed extract some useful spatial information with helps the model to train faster, while spatial permutation forces the model to ignore spatial patterns and make predictions only from spectral densities.

6.1.2 Choosing between temporal and spectral features

It can be seen from Figure 5.3, that power-only models minimize their loss faster than time-only models, which is especially visible for the RR patient: the time-only model was not able to train at all, while the power-only model decreased loss considerably and even overfit. For the BP patient, loss change is also ~ 2 times bigger in the power-only model rather than in the time-only model. In sum, power-only models can be considered to extract wider range of informative features. This is consistent with findings of Lu et al. (2017).

A further explanation of why the time-only model on RR data performed much worse than on BP data may be hidden in the RR patient's activation maps. RR patient had no significant activation in high-frequency power during motor imagery tasks (see Fig. A.8). Moreover, all predictions were of "rest" class, which is over-represented in data. When ANN models cannot efficiently lower their loss (cannot learn new features), they tend to predict a single class for all data samples. In the case of the RR model, it may indicate that as the time-only model cannot train, it is concentrating on high frequencies (narrow peaks visible on temporal data) while ignoring lower frequencies which are difficult to see in temporal data.

6.1.3 Using temporal and spectral features together

It was expected for time-power models to have the best result because of the largest number of features; however, they train even slower than time-only models (see Fig. 5.3). This is logical, as time-power models have a lot more weights and data (data samples were 24 times larger than time-only samples, and 100 times larger than power-only samples), so they need more time to converge. Time-power models might outrace the power-only model after enough training epochs, but this assumption needs to be checked and requires either more time or computational power. The full potential of time-power models was not analyzed in this work, as time-power models were too long to train: while time-only models completed one epoch in 22 s, and power-only models in 30 s, time-power models needed almost 11 min for one epoch on the same machine. This makes time-power models more difficult to analyze and tune. Further pre-training feature selection needs to be done to make data smaller.

6.2 Comparing predictions of different patient data

6.2.1 Discriminating between hand and tongue imagined movements

From the overlap metrics between hand and tongue tasks (see Table 5.1), it was found that there are significant overlaps between tasks in both motor and imagery activity, but overlaps were less significant for high-frequency activation maps, on average. This matches previous calculations on the same data (Miller et al., 2010). Still, this was not true for all patients: for example, patient BP has no significant overlap for either task group, while patient FP has a significant overlap for each task group. Nevertheless, after calculating prediction metrics for both BP and FP patients, it was found that power-only model prediction accuracy is similarly low for these two patients (56 % for BP and 54 % for FP) while predicting motor imagery. Overall, although models showed the ability to minimize their loss, more epochs are need to be trained to find the limit of the models' prediction power.

6.2.2 Understanding which features are informative in training

It would be beneficial to estimate whether prediction accuracy correlates with any activation overlap to better understand which data features affect the training speed the most; but it should be done with models trained for a longer time, so the differences between models would become more significant. This can be done in future work.

Instead, trained model weights for trained power-only models were visualized to estimate which frequencies were of the first importance for models. The visualization is provided in Figure A.9. It can be seen how different models changed their weights in the first 50 epochs. The third kernel rows immediately catch the eye: although the BP model performed better than the HH model, they both have constant values in the third kernel row, so it is unclear why both models chose to average their third kernel rows.

Additionally, the fourth rows of BP and RR models look similar, which have high weight values in the first columns and lower weight values in the last columns. On the contrary, the HH model has higher weights in the last columns and lower weights in the first columns. This difference may be one of the reasons for worse HH model performance.

Again, longer trained and better fit models can show specific patterns in their layer weights, which can assist in better pre-training feature extraction. Future work would be evaluating differences between kernels, from which model tuning would also benefit.

6.2.3 One-patient models vs. two-patient models

Two-patient models were compared with respective one-patient models. An example with predicting motor action for RR patient is provided in Figure 6.1, and for FP patient in Figure 6.2. For the RR patient, all three confusion matrices look nearly identical, but this is not the case for the FP patient:

- FP+JM model scored 70 % accuracy on predicting FP motor actions, which is noticeably higher compared to the FP model (which has 55 %). FP-JM model has much better precision from "hand" class (70 % compared to 43 %) and recall (78 % compared to 54 %). It means that JM data boosted the recognition of this class for the FP patient. This is an example where joining two patients in one training set is beneficial.

- On the contrary, the FP+RR model performed badly on FP data, achieving 56 % accuracy (close to the FP model). Here, "hand" class also get increased attention, but it is over-predicted, as its precision is only 41 % even though it has the same recall as in FP+JM (78 %). This is an example of worsening model performance when joining two patients in one training set. An

interesting point is that this negative effect is much stronger than for JM+RR pair which have no activation overlap.

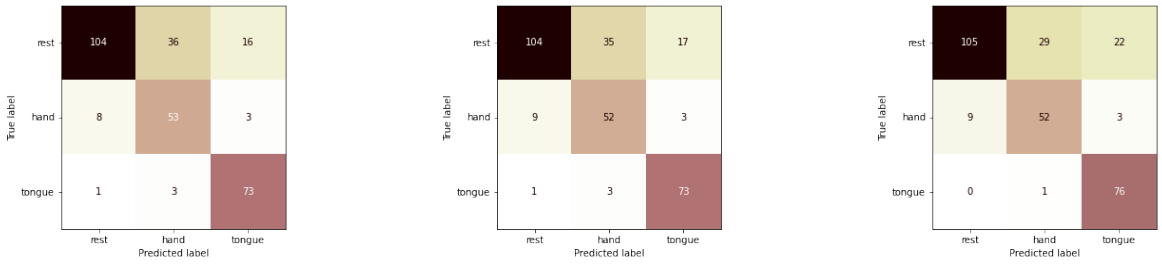

(a) RR (b) JM+RR (c) FP+RR

Figure 6.1: Confusion matrices for predictions made on RR patient motor action data, while using different trained models (training data is named under the matrices).

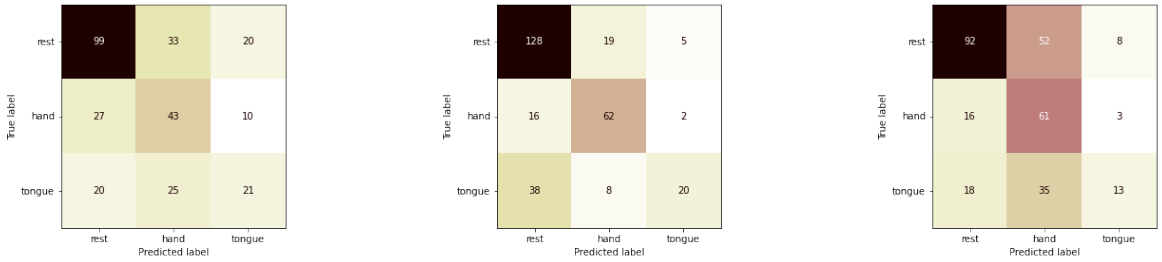

(a) FP (b) FP+JM (c) FP+RR

Figure 6.2: Confusion matrices for predictions made on FP patient motor action data, while using different trained models (training data is named under the matrices).

After further analyzing the connection between FP+JM and FP+RR pairs, it was noticed that FP has hand activation overlap with both JM and RR in low frequencies (and the overlap with RR patient is higher), while only with JM in high frequencies. Furthermore, this high-frequency activation overlap is the biggest of all found overlaps altogether. A conclusion can be made that higher frequencies are more specific and better for recognizing specific movements, while lower frequencies can instead confuse the model.

6.2.4 Cross-testing on different patients

Overall, higher accuracy models still show accuracy close to baseline when used to make predictions from a different patient rather than the one used in the training (see Fig. 5.10). It means that models tend to overfit against the patient and the difference between patients is considerably strong. On the other hand, training a unified model for all patients together can be a promising future work.

6.3 Changing between motor imagery and motor action

6.3.1 Comparing motor imagery and motor action predictions

From the overlap metrics shown in Figure 5.8, most overlapping activation maps between patients are low-frequency motor action maps; there is a lesser overlap between motor imagery in high-frequency

power.

Models which trained on motor action (see Fig. 5.11) show a bigger loss change (∼2 times in both BP and RR patients) compared to motor imagery models, although this change slows down in later epochs. Even more importantly, test loss changes are also lower in motor action models. Four out of seven models trained on motor action (for BP, JC, JM, and RR patients) got an accuracy of 69 % or higher. All other models, as well as motor imagery models, performed with accuracy close to the baseline. In conclusion, motor imagery is indeed less visible in data compared to motor action.

6.3.2 Predicting motor imagery from motor action

After calculating activation maps and overlap between motor imagery and motor action (see Table 5.3), the results were in agreement with the ones presented in Miller et al. (2010). Most of the patients had significant overlaps in all task groups and frequency ranges, the main exception being the BP patient. No significant overlap was found for them in either group. A possible explanation is that this patient had difficulties with imagery tasks. Nevertheless, the models for this patient performed similarly to other patients. It means although BP had different activation patterns for motor imagery and motor action, the temporal and spectral features were of the same difference between different tasks, as in other patients.

When motor action models were used to predict motor imagery, they show very similar results as models trained on motor imagery (see Fig. 6.3). Furthermore, motor action model under-predicts "tongue" class. Knowing that for the RR patient, there is no significant activation for both hand and tongue motor imagery, it can be concluded that the motor action model predicts "tongue" class mostly from higher frequency patterns, which are absent in motor imagery, while for "hand" class, lower frequency patterns are also considered (F1 scores are 48 % and 8 % for hand and tongue respectively, compared to 49 % and 39 % from motor imagery model). The Imagery+Action RR model shows even worse results (47 % accuracy and over-prediction of "hand" class).

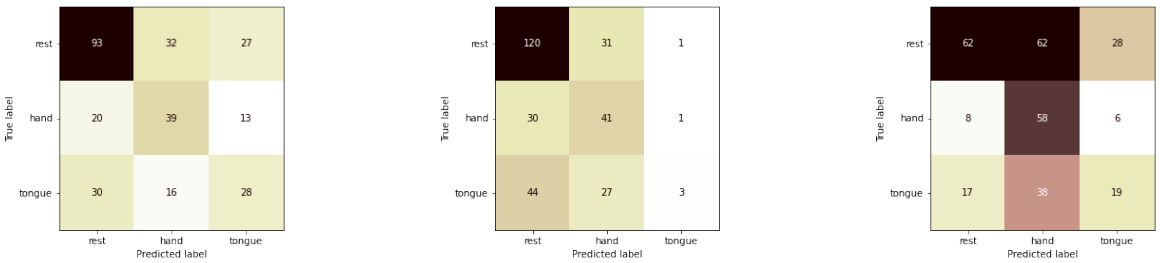

(a) Imagery (b) Action (c) Imagery+Action

Figure 6.3: Confusion matrices for predictions made on RR patient motor imagery data, while using different trained models (training data is named under the matrices).

Overall, using motor action models to predict motor imagery has shown worse results that using motor imagery models (see Fig. 5.10 (a) and (c)). Two notable exceptions exists:

1. HH patient got 56 % accuracy when using the motor action model to predict motor imagery. Using the motor imagery model resulted in a much lower 34 %. Although the assumption is made that using a motor action model for motor imagery prediction is beneficial for these patients, accuracy is too low for definitive results.

2. RR patient had 54 % and 55 % accuracy for predicting from motor imagery and motor action, respectively, being the only patient who got similar accuracy between these two models. Still, the accuracy is close to the baseline, and no decisive conclusions can be drawn.

An initial conclusion can be made that using motor action data to predict motor imagery is not beneficial and even disadvantageous. Longer training of models can verify this conclusion.

6.4 Using the pipeline with another data set

6.4.1 Real-time models

In sum, multi-class models with window-based data fragmentation show much slower convergence in BP and RR patients (see Fig. 5.12). Changes in model architecture can lead to more accurate predictions. Furthermore, if predictions should capture the time moment when the change happened, then other types of ANN models may be more beneficial, e.g. which can extract additional information from the memory of previous data samples. The training of such models was out of the scope of this work, but it needs to be researched in the future.

6.4.2 Finding motor imagery in REM sleep data

Overall, the predictions on REM sleep data were in disagreement between models REM sleep data (see Table 5.4). First of all, the overall percentage of "rest" class is in 72 - 96 % range, which is sensible. The difference between "hand" and "tongue" prediction percentage varies from -10.6 % to 11.6 % ("hand" is predicted 2.75 % more often in average).

Some models simply over-predicted one class (JM model did this on all REM sleep data patients). Some models never predicted one class (e.g. the FP model has not found any tongue movement, and the RH model - hand movement). Knowing that and the fact that all models used for prediction have accuracy close to the baseline, no conclusions can be drawn from these predictions.

There were only 25 fragments in total for which all models predicted the same class, but it was only "rest" class because the JM model has not predicted any other classes. When looking for "hand" or "tongue" class, the maximum number of models with the same predictions was four. Two fragments were found this way. Both fragments belong to patient nr. 106, with BP, FP, HH, and RR models predicted "hand" class. Fragments are visualized in Figure A.10 together with one "rest"-predicted fragment (by six models). No noticeable difference between "hand" and "rest" fragments was seen in both temporal and spectral representation, leaving it a task for a ECoG and REM specialist to check how close predictions can be to the truth.

Other than the absence of ground truth, two serious limitations were found during this task: first, if frequencies as high as 100 Hz are used as features, the data should be sampled at least by 200 Hz, but additional data simplifying such as window averaging may result in requiring even higher sample rates. For instance, motor data fragments had 100 temporal features, which were calculated from 200 ms fragments sampled at 1000 Hz. REM sleep data, on the other hand, was sampled at 200 Hz, meaning for it to have the same resolution, temporal space needs to be reduced to 20 features. This results in different sizes of data samples, which are incompatible with pre-trained models. As a result, fragments were cropped into bigger time ranges. For power-only models, this is not a big problem, but for models which train from temporal data, the initial training data should be downsampled to be compatible with a bigger number of ECoG data sets.

Another problem, specific to dream decoding, is the abundance of REMs during REM sleep. Ocular activity may introduce additional noise into the data, especially if electrodes are placed near the eyes, and confuse the models trained on data with less ocular activity. Removing possible ocular activity artifacts is an important step that was out of scope for this work, but should be addressed in future work.

Nevertheless, it was shown that there is the possibility to train a model and then use it on ECoG data collected from different patients in different conditions. Using the pipeline written during this

work, training, testing and predictions can be done a relatively simple and fast way while leaving opportunities for customization. The accessibility of this pipeline will help analyze ECoG data more efficiently and continue the research on the reaDream project.

6.5 Other limitations and future work

All patients from motor data had medically refractory epilepsy, which could affect the functional areas of their brain. Moreover, some of them described having difficulties during imagery tasks. All these facts raise the chance that the data is not fit for training a model on it, as it can incorrectly reflect the brain activity of healthy humans. Other considerations are raised from the fact that seizure activity was not filtered from the data. Although it can affect model training, as fragments with seizures do not represent activation from motor tasks, this effect should be minimal, as seizures happen randomly, while motor activity is present in all respective fragments. In future studies, the impact of seizures on predicting motor activity can be studied.

Another possible problem is the mapping of electrode positions: electrodes were mapped to a standardized brain, but brains can be of different shapes and sizes, which can introduce additional errors into electrode locations (e.g. some electrodes were mapped outside of the brain as it was shown above). These errors can become significant after simplifying locations.

A serious limitation for deep ANNs is time consumption. As it was noted before, time-power models, trained on much bigger data samples, consumed 20 times more time for one epoch, compared to models which used smaller data samples. This makes it difficult to train a good model in time, as choosing the best architecture and hyper-parameters needs validation by training at least 3-5 epochs. Using Adam or a similar optimizer with much faster convergence adds to the problem, as the loss change from Adam can be much more unstable compared to more slow but steady SGD, so even more epochs may be needed to better see whether the model performs better. Additionally, cross-validation and validation with different seeds should be performed to ensure that the results are reproducible. This will further increase the time requirement.

Although CNNs can detect spatial patterns which is beneficial for multi-electrode brain activity recordings, they do not have a memory of previous samples, which can provide valuable information in real-time prediction settings. Recurrent Neural Networks, such as Long-Short Term Memory models, are more fit for real-time decoding, as they also see the context of a sample. Although these models are mostly used for natural language processing tasks such as speech recognition or generation, a way to use them for decoding dreamed activities can be thought of. The view of motor action/imagery as a "sentence" of simplest movements (flexion/extension of specific muscles and joints) supports the idea of adjusting a natural language model to decode such activity. On the other hand, dreamed movements can be unusual or illogical, which makes their context a somewhat less useful predictor. Nevertheless, future work can be on coding motor action into sub-components and forming motor action "sentences", which can better represent continuous and complex motor activity.

Additionally, as new ANN models are constantly developed, deeper research of cutting-edge ANN methods and techniques can help to increase model efficiency. The main limitation is that modern ANN models with exceptional accuracy tend to require substantial computational power, or their training can last days and months. That is why it can be more beneficial to pre-extract some specific features from the data for training, rather than using huge ANNs which could do the extraction automatically. Furthermore, simpler ML algorithms should not be neglected, such as Support Vector Machines, which also have the potential to predict motor imagery.

Lastly, other cognitive and perceptional phenomena which might happen during dreaming can also be evaluated for the current potential of their decoding. As new data sets become openly available, new models can be trained on them, providing valuable insights into both better data transformations and efficient model architectures. While adding more motor data to the current collection, new ways

of data generalization can be researched together with finding common activation patterns for different movements for their later detection in dream data.

CONCLUSIONS

A pipeline for electrode location inclusion into the data was designed, which allows joining data from several patients with differently placed ECoG grids. ANN models with either one or two CNN layers were developed and trained with different data sets. Three data representations were used to compare their impact on training speed. The main conclusions are:

1. Incorporating spatial information about electrode localization helps models both train faster and be used with different patients, and spectral features help models learn faster compared to temporal features, as they provide more information.

2. Model cross-testing shows low accuracy when predicting movements using a model trained on another patient, but two-patient models can both increase and decrease prediction accuracy for patients in pair compared with when trained alone.

3. Motor action is easier discriminated than motor imagery, although it is noticeable not in all patients; however, using motor action or imagery+action models to predict motor imagery results in worse accuracy than predicting when motor imagery models.

4. Predicting motor imagery from dreams requires a real-time approach, but different model architectures are needed for this task.

The code written and used for this work is published in an open repository: https://github.com/Tallivm/readream-motor.

A video summarizing the reaDream idea was accepted to the HCI International 2022 Conference and can be found by link: https://www.youtube.com/watch?v=FZZuVqiJpzQ. The paper titled "Training CNN to detect motor imagery in ECoG data recorded during dreaming" was submitted to the same Conference. Skills acquired during working on the Thesis were applied during the virtual BR41N.IO Hackathon 2022.

REFERENCES

Aydemir, Ö., & Kayikçioğlu, T. (2010). Motor imagery ECoG signals classification using wavelet transform features [ISSN: 2165-0608]. 2010 IEEE 18th Signal Processing and Communications Applications Conference, 296–299. https://doi.org/10.1109/SIU.2010.5652130

Barone, D. A., & Henchcliffe, C. (2018). Rapid eye movement sleep behavior disorder and the link to alpha-synucleinopathies. Clinical neurophysiology : official journal of the International Federation of Clinical Neurophysiology, 129(8), 1551–1564. https://doi.org/10.1016/j.clinph.2018.05.003

Batula, A. M., Mark, J. A., Kim, Y. E., & Ayaz, H. (2017). Comparison of brain activation during motor imagery and motor movement using fNIRS. Computational Intelligence and Neuroscience, 2017, 5491296. https://doi.org/10.1155/2017/5491296

Beaulieu-Prévost, D., & Zadra, A. (2015). When people remember dreams they never experienced: A study of the malleability of dream recall over time [Place: US Publisher: Educational Publishing Foundation]. Dreaming, 25(1), 18–31. https://doi.org/10.1037/a0038788

Bhandari, A., Koppen, J., & Agzarian, M. (2020). Convolutional neural networks for brain tumour segmentation. Insights into Imaging, 11(1), 77. https://doi.org/10.1186/s13244-020-00869-4

Blake, Y., Terburg, D., Balchin, R., van Honk, J., & Solms, M. (2019). The role of the basolateral amygdala in dreaming. Cortex, 113, 169–183. https://doi.org/10.1016/j.cortex.2018.12.016

Blakely, T., Miller, K. J., Rao, R. P. N., Holmes, M. D., & Ojemann, J. G. (2008). Localization and classification of phonemes using high spatial resolution electrocorticography (ECoG) grids [Publisher: Annu Int Conf IEEE Eng Med Biol Soc]. Annual International Conference of the IEEE Engineering in Medicine and Biology Society. IEEE Engineering in Medicine and Biology Society. Annual International Conference, 2008. https://doi.org/10.1109/IEMBS.2008.4650328

Caldwell, D. J., Ojemann, J. G., & Rao, R. P. N. (2019). Direct electrical stimulation in electrocorticographic brain-computer interfaces: Enabling technologies for input to cortex. Frontiers in Neuroscience, 13, 804. https://doi.org/10.3389/fnins.2019.00804

Carr, M., & Nielsen, T. (2015). Daydreams and nap dreams: Content comparisons. Consciousness and Cognition, 36, 196–205. https://doi.org/10.1016/j.concog.2015.06.012

Caucheteux, C., & King, J.-R. (2022). Brains and algorithms partially converge in natural language processing [Number: 1 Publisher: Nature Publishing Group]. Communications Biology, 5(1), 1–10. https://doi.org/10.1038/s42003-022-03036-1

Caviglia, G. (2021). Working on dreams, from neuroscience to psychotherapy. Research in Psychotherapy : Psychopathology, Process, and Outcome, 24(2), 540. https://doi.org/10.4081/ripppo.2021.540

Cheng, Q., Kaplan, A. D., Karande, P., Bijanzadeh, M., Dawes, H., & Chang, E. (2019). Emotion discrimination through electrode network connectivity pattern recognition [ISSN: 2576-2303]. 2019 53rd Asilomar Conference on Signals, Systems, and Computers, 2139–2143. https://doi.org/10.1109/IEEECONF44664.2019.9049060

Chiong, W., Leonard, M. K., & Chang, E. F. (2018). Neurosurgical patients as human research subjects: Ethical considerations in intracranial electrophysiology research. Neurosurgery, 83(1), 29–37. https://doi.org/10.1093/neuros/nyx361

Choi, H., Lee, J., Park, J., Cho, B. H., Lee, K.-M., & Jang, D. P. (2018). Movement state classification for bimanual BCI from non-human primate's epidural ECoG using three-dimensional

convolutional neural network [ISSN: 2572-7672]. 2018 6th International Conference on Brain-Computer Interface (BCI), 1–3. https://doi.org/10.1109/IWW-BCI.2018.8311534

Dahm, S. F., & Rieger, M. (2016). Is there symmetry in motor imagery? exploring different versions of the mental chronometry paradigm. Attention, Perception, & Psychophysics, 78(6), 1794–1805. https://doi.org/10.3758/s13414-016-1112-9

Deshpande, A., Estrela, V. V., & Patavardhan, P. (2021). The DCT-CNN-ResNet50 architecture to classify brain tumors with super-resolution, convolutional neural network, and the ResNet50. Neuroscience Informatics, 1(4), 100013. https://doi.org/10.1016/j.neuri.2021.100013

Dresler, M., Koch, S. P., Wehrle, R., Spoormaker, V. I., Holsboer, F., Steiger, A., Sämann, P. G., Obrig, H., & Czisch, M. (2011). Dreamed movement elicits activation in the sensorimotor cortex. Current biology: CB, 21(21), 1833–1837. https://doi.org/10.1016/j.cub.2011.09.029

Eagleman, D. M., & Vaughn, D. A. (2021). The defensive activation theory: REM sleep as a mechanism to prevent takeover of the visual cortex. Frontiers in Neuroscience, 15.

Erlacher, D., & Schredl, M. (2008). Do REM (lucid) dreamed and executed actions share the same neural substrate? International Journal of Dream Research, 7–14. https://doi.org/10.11588/ijodr.2008.1.20

Fosse, R., & Larøi, F. (2020). Quantifying auditory impressions in dreams in order to assess the relevance of dreaming as a model for psychosis [Publisher: Public Library of Science]. PLOS ONE, 15(3), e0230212. https://doi.org/10.1371/journal.pone.0230212

Frauscher, B., Joshi, S., von Ellenrieder, N., Nguyen, D. K., Dubeau, F., & Gotman, J. (2018). Sharply contoured theta waves are the human correlate of ponto-geniculo-occipital waves in the primary visual cortex. Clinical Neurophysiology: Official Journal of the International Federation of Clinical Neurophysiology, 129(8), 1526–1533. https://doi.org/10.1016/j.clinph.2018.04.605

González, J., Cavelli, M., Mondino, A., Pascovich, C., Castro-Zaballa, S., Torterolo, P., & Rubido, N. (2019). Decreased electrocortical temporal complexity distinguishes sleep from wakefulness [Number: 1 Publisher: Nature Publishing Group]. Scientific Reports, 9(1), 18457. https://doi.org/10.1038/s41598-019-54788-6

Gott, J. A., Liley, D. T. J., & Hobson, J. A. (2017). Towards a functional understanding of PGO waves. Frontiers in Human Neuroscience, 11, 89. https://doi.org/10.3389/fnhum.2017.00089

Haar Horowitz, A., Cunningham, T. J., Maes, P., & Stickgold, R. (2020). Dormio: A targeted dream incubation device. Consciousness and Cognition, 83, 102938. https://doi.org/10.1016/j.concog.2020.102938

Haufe, S., DeGuzman, P., Henin, S., Arcaro, M., Honey, C. J., Hasson, U., & Parra, L. C. (2018). Elucidating relations between fMRI, ECoG, and EEG through a common natural stimulus. NeuroImage, 179, 79–91. https://doi.org/10.1016/j.neuroimage.2018.06.016

He, K., Zhang, X., Ren, S., & Sun, J. (2015). Delving deep into rectifiers: Surpassing human-level performance on ImageNet classification. arXiv:1502.01852 [cs].

Herlin, B., Leu-Semenescu, S., Chaumereuil, C., & Arnulf, I. (2015). Evidence that non-dreamers do dream: A REM sleep behaviour disorder model. Journal of Sleep Research, 24(6), 602–609. https://doi.org/10.1111/jsr.12323

Hilditch, C. J., & McHill, A. W. (2019). Sleep inertia: Current insights. Nature and Science of Sleep, 11, 155–165. https://doi.org/10.2147/NSS.S188911

Hill, N. J., Gupta, D., Brunner, P., Gunduz, A., Adamo, M. A., Ritaccio, A., & Schalk, G. (2012). Recording human electrocorticographic (ECoG) signals for neuroscientific research and real-time functional cortical mapping. Journal of Visualized Experiments: JoVE, (64), 3993. https://doi.org/10.3791/3993

Hobson, J. A. (2009). REM sleep and dreaming: Towards a theory of protoconsciousness [Number: 11 Publisher: Nature Publishing Group]. Nature Reviews Neuroscience, 10(11), 803–813. https://doi.org/10.1038/nrn2716

Holler, S., Köstinger, G., Martin, K. A. C., Schuhknecht, G. F. P., & Stratford, K. J. (2021). Structure and function of a neocortical synapse [Number: 7848 Publisher: Nature Publishing Group]. Nature, 591(7848), 111–116. https://doi.org/10.1038/s41586-020-03134-2

Horikawa, T., Tamaki, M., Miyawaki, Y., & Kamitani, Y. (2013). Neural decoding of visual imagery during sleep [Publisher: American Association for the Advancement of Science]. Science, 340(6132), 639–642. https://doi.org/10.1126/science.1234330

Horton, C. L. (2017). Consciousness across sleep and wake: Discontinuity and continuity of memory experiences as a reflection of consolidation processes. Frontiers in Psychiatry, 8.

Imbiriba, L. A., Joffily, S. B., Rodrigues, E. C., & Vargas, C. D. (2010). Blindness and motor imagery. The neurophysiological foundations of mental and motor imagery. Oxford University Press. https://doi.org/10.1093/acprof:oso/9780199546251.003.0013

Izawa, S., Chowdhury, S., Miyazaki, T., Mukai, Y., Ono, D., Inoue, R., Ohmura, Y., Mizoguchi, H., Kimura, K., Yoshioka, M., Terao, A., Kilduff, T. S., & Yamanaka, A. (2019). REM sleep–active MCH neurons are involved in forgetting hippocampus-dependent memories [Publisher: American Association for the Advancement of Science]. Science, 365(6459), 1308–1313. https://doi.org/10.1126/science.aax9238

Jahangiri, F. R., Chima, G. S., Pearson, M., Jackson, J., & Siddiqui, A. A. (2021). Mapping of the language cortex. Cureus, 13(5), e14960. https://doi.org/10.7759/cureus.14960

Kaiju, T., Doi, K., Yokota, M., Watanabe, K., Inoue, M., Ando, H., Takahashi, K., Yoshida, F., Hirata, M., & Suzuki, T. (2017). High spatiotemporal resolution ECoG recording of somatosensory evoked potentials with flexible micro-electrode arrays. Frontiers in Neural Circuits, 11.

Kanari, L., Ramaswamy, S., Shi, Y., Morand, S., Meystre, J., Perin, R., Abdellah, M., Wang, Y., Hess, K., & Markram, H. (2019). Objective morphological classification of neocortical pyramidal cells. Cerebral Cortex, 29(4), 1719–1735. https://doi.org/10.1093/cercor/bhy339

Kanaya, K., Mitsuhashi, T., Kiuchi, T., & Kobayashi, S. (2021). The efficacy of intraoperative passive language mapping for glioma surgery: A case report. Frontiers in Neurology, 12, 652401. https://doi.org/10.3389/fneur.2021.652401

Klinzing, J. G., Niethard, N., & Born, J. (2019). Mechanisms of systems memory consolidation during sleep [Number: 10 Publisher: Nature Publishing Group]. Nature Neuroscience, 22(10), 1598–1610. https://doi.org/10.1038/s41593-019-0467-3

Konkoly, K. R., Appel, K., Chabani, E., Mangiaruga, A., Gott, J., Mallett, R., Caughran, B., Witkowski, S., Whitmore, N. W., Mazurek, C. Y., Berent, J. B., Weber, F. D., Türker, B., Leu-Semenescu, S., Maranci, J.-B., Pipa, G., Arnulf, I., Oudiette, D., Dresler, M., & Paller, K. A. (2021). Real-time dialogue between experimenters and dreamers during REM sleep. Current biology: CB, 31(7), 1417–1427.e6. https://doi.org/10.1016/j.cub.2021.01.026

Korostenskaja, M., Kamada, K., Guger, C., Salinas, C., Westerveld, M., Castillo, E., Salillas, E., Chen, P.-C., Harris, E., Seddon, I., Elsayed, M., Kapeller, C., Schaal, A., Seo, J.-H., Baumgartner, J., & Lee, K. H. (2015). Electrocorticography-based real-time functional mapping for pediatric epilepsy surgery. Journal of Pediatric Epilepsy, 4. https://doi.org/10.1055/s-0035-1563728

Kovach, C. K., Tsuchiya, N., Kawasaki, H., Oya, H., Howard, M. A., & Adolphs, R. (2011). Manifestation of ocular-muscle EMG contamination in human intracranial recordings. NeuroImage, 54(1), 213–233. https://doi.org/10.1016/j.neuroimage.2010.08.002

Lai, G., Langevin, J.-P., Koek, R. J., Krahl, S. E., Bari, A. A., & Chen, J. W. Y. (2020). Acute effects and the dreamy state evoked by deep brain electrical stimulation of the amygdala: Associations of the amygdala in human dreaming, consciousness, emotions, and creativity. Frontiers in Human Neuroscience, 14.

Lancaster, J. L., Tordesillas-Gutiérrez, D., Martinez, M., Salinas, F., Evans, A., Zilles, K., Mazziotta, J. C., & Fox, P. T. (2007). Bias between MNI and talairach coordinates analyzed using the

ICBM-152 brain template. Human Brain Mapping, 28(11), 1194–1205. https://doi.org/10.1002/hbm.20345

Leske, S., & Dalal, S. S. (2019). Reducing power line noise in EEG and MEG data via spectrum interpolation. NeuroImage, 189, 763–776. https://doi.org/10.1016/j.neuroimage.2019.01.026

Leuthardt, E. C., Moran, D. W., & Mullen, T. R. (2021). Defining surgical terminology and risk for brain computer interface technologies. Frontiers in Neuroscience, 15, 599549. https://doi.org/10.3389/fnins.2021.599549

Liu, D., & Dan, Y. (2019). A motor theory of sleep-wake control: Arousal-action circuit. Annual Review of Neuroscience, 42, 27–46. https://doi.org/10.1146/annurev-neuro-080317-061813

Liu, Y., Coon, W. G., Pesters, A. d., Brunner, P., & Schalk, G. (2015). The effects of spatial filtering and artifacts on electrocorticographic signals [Publisher: IOP Publishing]. Journal of Neural Engineering, 12(5), 056008. https://doi.org/10.1088/1741-2560/12/5/056008

Lu, N., Li, T., Ren, X., & Miao, H. (2017). A deep learning scheme for motor imagery classification based on restricted boltzmann machines [Conference Name: IEEE Transactions on Neural Systems and Rehabilitation Engineering]. IEEE Transactions on Neural Systems and Rehabilitation Engineering, 25(6), 566–576. https://doi.org/10.1109/TNSRE.2016.2601240

Mahowald, M. W., & Schenck, C. H. (2011). Chapter 95 - REM sleep parasomnias. In M. H. Kryger, T. Roth, & W. C. Dement (Eds.), Principles and practice of sleep medicine (fifth edition) (pp. 1083–1097). W.B. Saunders. https://doi.org/10.1016/B978-1-4160-6645-3.00095-5

Maquet. (2000). Functional neuroimaging of normal human sleep by positron emission tomography. Journal of Sleep Research, 9(3), 207–231. https://doi.org/10.1046/j.1365-2869.2000.00214.x

Martin, J. M., Andriano, D. W., Mota, N. B., Mota-Rolim, S. A., Araújo, J. F., Solms, M., & Ribeiro, S. (2020). Structural differences between REM and non-REM dream reports assessed by graph analysis [Publisher: Public Library of Science]. PLOS ONE, 15(7), e0228903. https://doi.org/10.1371/journal.pone.0228903

Meng, L., & Xiang, J. (2018). Brain network analysis and classification based on convolutional neural network. Frontiers in Computational Neuroscience, 12.

Miller, K. J., Hermes, D., & Staff, N. P. (2020). The current state of electrocorticography-based brain-computer interfaces. Neurosurgical Focus, 49(1), E2. https://doi.org/10.3171/2020.4.FOCUS20185

Miller, K. J., Schalk, G., Fetz, E. E., Nijs, M. d., Ojemann, J. G., & Rao, R. P. N. (2010). Cortical activity during motor execution, motor imagery, and imagery-based online feedback [Publisher: National Academy of Sciences Section: Biological Sciences]. Proceedings of the National Academy of Sciences, 107(9), 4430–4435. https://doi.org/10.1073/pnas.0913697107

Miller, K. J. (2016). A library of human electrocorticographic data and analyses - research from stanford university - spotlight at stanford. Retrieved February 17, 2022, from https://exhibits.stanford.edu/data/catalog/zk881ps0522

Moon, S.-E., Jang, S., & Lee, J.-S. (2018). Convolutional neural network approach for eeg-based emotion recognition using brain connectivity and its spatial information [ISSN: 2379-190X]. 2018 IEEE International Conference on Acoustics, Speech and Signal Processing (ICASSP), 2556–2560. https://doi.org/10.1109/ICASSP.2018.8461315

Moses, D. A., Metzger, S. L., Liu, J. R., Anumanchipalli, G. K., Makin, J. G., Sun, P. F., Chartier, J., Dougherty, M. E., Liu, P. M., Abrams, G. M., Tu-Chan, A., Ganguly, K., & Chang, E. F. (2021). Neuroprosthesis for decoding speech in a paralyzed person with anarthria. The New England Journal of Medicine, 385(3), 217–227. https://doi.org/10.1056/NEJMoa2027540

Mota, N. B., Furtado, R., Maia, P. P. C., Copelli, M., & Ribeiro, S. (2014). Graph analysis of dream reports is especially informative about psychosis [Number: 1 Publisher: Nature Publishing Group]. Scientific Reports, 4(1), 3691. https://doi.org/10.1038/srep03691

Motor cortex (section 3, chapter 3) neuroscience online: An electronic textbook for the neurosciences | department of neurobiology and anatomy - the university of texas medical school at houston. (n.d.). Retrieved May 2, 2022, from https://nba.uth.tmc.edu/neuroscience/m/s3/chapter03.html

Musk, E., & Neuralink. (2019). An integrated brain-machine interface platform with thousands of channels [Company: Journal of Medical Internet Research Distributor: Journal of Medical Internet Research Institution: Journal of Medical Internet Research Label: Journal of Medical Internet Research Publisher: JMIR Publications Inc., Toronto, Canada]. Journal of Medical Internet Research, 21(10), e16194. https://doi.org/10.2196/16194

Nir, Y., & Tononi, G. (2010). Dreaming and the brain: From phenomenology to neurophysiology. Trends in Cognitive Sciences, 14(2), 88–100. https://doi.org/10.1016/j.tics.2009.12.001

Noreika, V., Windt, J. M., Kern, M., Valli, K., Salonen, T., Parkkola, R., Revonsuo, A., Karim, A. A., Ball, T., & Lenggenhager, B. (2020). Modulating dream experience: Noninvasive brain stimulation over the sensorimotor cortex reduces dream movement [Number: 1 Publisher: Nature Publishing Group]. Scientific Reports, 10(1), 6735. https://doi.org/10.1038/s41598-020-63479-6

Oxley, T. J., Yoo, P. E., Rind, G. S., Ronayne, S. M., Lee, C. M. S., Bird, C., Hampshire, V., Sharma, R. P., Morokoff, A., Williams, D. L., MacIsaac, C., Howard, M. E., Irving, L., Vrljic, I., Williams, C., John, S. E., Weissenborn, F., Dazenko, M., Balabanski, A. H., … Opie, N. L. (2021). Motor neuroprosthesis implanted with neurointerventional surgery improves capacity for activities of daily living tasks in severe paralysis: First in-human experience. Journal of NeuroInterventional Surgery, 13(2), 102–108. https://doi.org/10.1136/neurintsurg-2020-016862

Pagel, J. F., & Kwiatkowski, C. F. (2003). Creativity and dreaming: Correlation of reported dream incorporation into waking behavior with level and type of creative interest. Creativity Research Journal, 15(2), 199–205. https://doi.org/10.1080/10400419.2003.9651412

Paller, K. A., Creery, J. D., & Schechtman, E. (2021). Memory and sleep: How sleep cognition can change the waking mind for the better. Annual Review of Psychology, 72, 123–150. https://doi.org/10.1146/annurev-psych-010419-050815

Pascarella, A., Todaro, C., Clerc, M., Serre, T., & Piana, M. (2016). Source modeling of Electro-CorticoGraphy (ECoG) data: Stability analysis and spatial filtering. Journal of Neuroscience Methods, 263, 134–144. https://doi.org/10.1016/j.jneumeth.2016.02.012

Paul, F., Schredl, M., & Alpers, G. W. (2015). Nightmares affect the experience of sleep quality but not sleep architecture: An ambulatory polysomnographic study. Borderline Personality Disorder and Emotion Dysregulation, 2, 3. https://doi.org/10.1186/s40479-014-0023-4

Pool, E.-M., Rehme, A. K., Fink, G. R., Eickhoff, S. B., & Grefkes, C. (2014). Handedness and effective connectivity of the motor system. NeuroImage, 99, 451–460. https://doi.org/10.1016/j.neuroimage.2014.05.048

Prakash, H. R., Korostenskaja, M., Lee, K., Baumgartner, J., Castillo, E., & Bagci, U. (2017). Automatic response assessment in regions of language cortex in epilepsy patients using ECoG-based functional mapping and machine learning. 2017 IEEE International Conference on Systems, Man, and Cybernetics (SMC), 519–524. https://doi.org/10.1109/SMC.2017.8122658

Rasch, B., & Born, J. (2013). About sleep's role in memory. Physiological Reviews, 93(2), 681–766. https://doi.org/10.1152/physrev.00032.2012

RaviPrakash, H., Korostenskaja, M., Castillo, E. M., Lee, K. H., Salinas, C. M., Baumgartner, J., Anwar, S. M., Spampinato, C., & Bagci, U. (2020). Deep learning provides exceptional accuracy to ECoG-based functional language mapping for epilepsy surgery. Frontiers in Neuroscience, 14, 409. https://doi.org/10.3389/fnins.2020.00409

Ruder, S. (2017). An overview of gradient descent optimization algorithms. arXiv:1609.04747 [cs].

Russell, B., & Han, J. (2016). Jean morlet and the continuous wavelet transform. 28, 15.

Sato, N., Matsumoto, R., Shimotake, A., Matsuhashi, M., Otani, M., Kikuchi, T., Kunieda, T., Mizuhara, H., Miyamoto, S., Takahashi, R., & Ikeda, A. (2021). Frequency-dependent cortical interactions during semantic processing: An electrocorticogram cross-spectrum analysis using a semantic space model. Cerebral Cortex (New York, N.Y.: 1991), 31(9), 4329–4339. https://doi.org/10.1093/cercor/bhab089

Schalk, G., Kapeller, C., Guger, C., Ogawa, H., Hiroshima, S., Lafer-Sousa, R., Saygin, Z. M., Kamada, K., & Kanwisher, N. (2017). Facephenes and rainbows: Causal evidence for functional and anatomical specificity of face and color processing in the human brain. 114(46), 12285–12290. https://doi.org/10.1073/pnas.1713447114

Shen, G., Horikawa, T., Majima, K., & Kamitani, Y. (2019). Deep image reconstruction from human brain activity [Publisher: Public Library of Science]. PLOS Computational Biology, 15(1), e1006633. https://doi.org/10.1371/journal.pcbi.1006633

Siclari, F., Baird, B., Perogamvros, L., Bernardi, G., LaRocque, J. J., Riedner, B., Boly, M., Postle, B. R., & Tononi, G. (2017). The neural correlates of dreaming [Number: 6 Publisher: Nature Publishing Group]. Nature Neuroscience, 20(6), 872–878. https://doi.org/10.1038/nn.4545

Simor, P., Horváth, K., Gombos, F., Takács, K. P., & Bódizs, R. (2012). Disturbed dreaming and sleep quality: Altered sleep architecture in subjects with frequent nightmares. European Archives of Psychiatry and Clinical Neuroscience, 262(8), 687–696. https://doi.org/10.1007/s00406-012-0318-7

Snyder, A. C., Morais, M. J., Willis, C. M., & Smith, M. A. (2015). Global network influences on local functional connectivity. Nature Neuroscience, 18(5), 736–743. https://doi.org/10.1038/nn.3979

Speth, C., & Speth, J. (2018). A new measure of hallucinatory states and a discussion of REM sleep dreaming as a virtual laboratory for the rehearsal of embodied cognition. Cognitive Science, 42(1), 311–333. https://doi.org/10.1111/cogs.12491

Speth, J., & Speth, C. (2016). Motor imagery in REM sleep is increased by transcranial direct current stimulation of the left motor cortex (c3). Neuropsychologia, 86, 57–65. https://doi.org/10.1016/j.neuropsychologia.2016.04.010

Stumbrys, T., Erlacher, D., Johnson, M., & Schredl, M. (2014). The phenomenology of lucid dreaming: An online survey. The American Journal of Psychology, 127(2), 191–204. https://doi.org/10.5406/amerjpsyc.127.2.0191

Stumbrys, T., Erlacher, D., Schädlich, M., & Schredl, M. (2012). Induction of lucid dreams: A systematic review of evidence. Consciousness and Cognition, 21(3), 1456–1475. https://doi.org/10.1016/j.concog.2012.07.003

Sun, P., Anumanchipalli, G. K., & Chang, E. F. (2020). Brain2char: A deep architecture for decoding text from brain recordings. Journal of Neural Engineering. https://doi.org/10.1088/1741-2552/abc742

Torontali, Z. A., Fraigne, J. J., Sanghera, P., Horner, R., & Peever, J. (2019). The sublaterodorsal tegmental nucleus functions to couple brain state and motor activity during REM sleep and wakefulness. Current biology: CB, 29(22), 3803–3813.e5. https://doi.org/10.1016/j.cub.2019.09.026

Valencia Garcia, S., Luppi, P.-H., & Fort, P. (2018). A particular medullary-spinal inhibitory pathway is recruited for the expression of muscle atonia during REM sleep [Publisher: SAGE Publications Ltd STM]. Journal of Experimental Neuroscience, 12, 1179069518808744. https://doi.org/10.1177/1179069518808744

Van Essen, D. C., Donahue, C. J., Coalson, T. S., & Glasser, M. F. (2019). Cerebral cortical folding, parcellation, and connectivity in humans, nonhuman primates, and mice [PNAS]. Retrieved February 28, 2022, from https://www.pnas.org/doi/abs/10.1073/pnas.1902299116

Vignal, J.-P., Maillard, L., McGonigal, A., & Chauvel, P. (2007). The dreamy state: Hallucinations of autobiographic memory evoked by temporal lobe stimulations and seizures. Brain: A Journal of Neurology, 130, 88–99. https://doi.org/10.1093/brain/awl329

von Ellenrieder, N., Gotman, J., Zelmann, R., Rogers, C., Nguyen, D. K., Kahane, P., Dubeau, F., & Frauscher, B. (2020). How the human brain sleeps: Direct cortical recordings of normal brain activity. Annals of Neurology, 87(2), 289–301. https://doi.org/10.1002/ana.25651

Voss, P., Thomas, M. E., Cisneros-Franco, J. M., & de Villers-Sidani, É. (2017). Dynamic brains and the changing rules of neuroplasticity: Implications for learning and recovery. Frontiers in Psychology, 8.

Wang, Y.-Q., Liu, W.-Y., Li, L., Qu, W.-M., & Huang, Z.-L. (2021). Neural circuitry underlying REM sleep: A review of the literature and current concepts. Progress in Neurobiology, 204, 102106. https://doi.org/10.1016/j.pneurobio.2021.102106

Yellapantula, S., Forseth, K., Tandon, N., & Aazhang, B. (2021). NetDI: Methodology elucidating the role of power and dynamical brain network features that underpin word production. eNeuro, 8(1), ENEURO.0177–20.2020. https://doi.org/10.1523/ENEURO.0177-20.2020

Zadra, A., & Domhoff, G. W. (2011). Chapter 50 - dream content: Quantitative findings. In M. H. Kryger, T. Roth, & W. C. Dement (Eds.), Principles and practice of sleep medicine (fifth edition) (pp. 585–594). W.B. Saunders. https://doi.org/10.1016/B978-1-4160-6645-3.00050-5

Zheng, W., Minama Reddy, G. K., Dai, F., Chandramani, A., Brang, D., Hunter, S., Kohrman, M. H., Rose, S., Rossi, M., Tao, J., Wu, S., Byrne, R., Frim, D. M., Warnke, P., & Towle, V. L. (2021). Chasing language through the brain: Successive parallel networks. Clinical Neurophysiology: Official Journal of the International Federation of Clinical Neurophysiology, 132(1), 80–93. https://doi.org/10.1016/j.clinph.2020.10.007

SUMMARY

Vilnius University

System Biology master program

Taisija Dėmčėnko

A Neural Network to Detect Motor Imagery in ECoG Data Recorded During Dreaming

Master Thesis

Abstract

People spend about one third of their lives sleeping and dreaming. Despite the impact of dreams on our emotions and memory, dreams are often forgotten. Motor imagery is one of the major components reported to be present in dreams, along with other sensory, perceptual, and cognitive phenomena. In our pursuit of developing an objective dream-content recording methodology, we focused on the motor imagery-related dream component. The recording of brain electromagnetic activity during sleep and the decoding of it with a machine learning (ML) model into dream components can be performed to collect detailed dream reports. However, the model needs training data, and dream contents cannot be controlled and are hidden from external observers. It has been shown that brain activation during dreamed actions corresponds to the brain activation for the same actions in a wakeful state, so training data can be collected from awake subjects. Electrocorticography (ECoG) data is rare and not generalized between subjects, so using it is problematic, as deep ML models are prone to overfit on little amounts of data. A way to generalize ECoG data to train a model on several subjects' data simultaneously is proposed in this work. A pipeline is used with ECoG data to develop a classifier that discriminates between hand and tongue movements in different patients. An emphasis is made on Convolutional Neural Network (CNN) models. A hypothesis is tested on whether a motor imagery classifier can be trained on real motor data, as such data is easier to collect. By training models on different data sets, it is shown that motor activity data is more easily discriminated compared to motor imagery. Spectral power features were shown to be more informative compared to temporal features. Finally, the model is used to predict motor imagery during Rapid Eye Movement (REM) sleep.

SUMMARY IN LITHUANIAN

Vilniaus Universitetas

Sistemų biologijos programa

Taisija Dėmčėnko

Įsivaizduojamo judesio aptikimas ECoG įrašuose sapnų metu pasitelkiant neuroninius tinklus

Magistro baigiamasis darbas

Santrauka

Maždaug trečdalį savo gyvenimo žmonės praleidžia miegodami ir sapnuodami. Nepaisant sapnų poveikio mūsų emocijoms ir atminčiai, sapnai dažnai pamirštami. Motoriniai vaizdai yra vienas iš pagrindinių komponentų, kurie, kaip teigiama, yra sapnuose, kartu su kitais jutiminiais, suvokimo ir kognityviniais reiškiniais. Siekdami sukurti objektyvią sapnų turinio įrašymo metodiką, daugiausia dėmesio skyrėme su motoriniais vaizdiniais susijusiam sapnų komponentui. Siekiant surinkti išsamius sapnų ataskaitas, galima įrašyti smegenų elektromagnetinį aktyvumą miego metu ir jį dekoduoti į sapnų komponentus naudojant mašininio mokymosi (MM) modelį. Tačiau modeliui reikia mokymo duomenų, o sapnų turinio negalima kontroliuoti ir jis yra paslėptas nuo išorinių stebėtojų. Buvo įrodyta, kad smegenų suaktyvėjimas sapnuojant atitinka smegenų suaktyvėjimą atliekant tuos pačius veiksmus budrumo būsenoje, todėl mokymo duomenis galima rinkti iš budrių tiriamųjų. Elektrokortikografijos (EKoG) duomenys yra reti ir nėra generalizuoti tarp tiriamųjų, todėl jų naudojimas yra problematiškas, nes gilieji MM modeliai yra linkę per daug prisitaikyti prie mažo duomenų kiekio. Šiame darbe siūlomas būdas apibendrinti EKoG duomenis, kad būtų galima vienu metu mokyti modelį pagal kelių subjektų duomenis. Naudojamas algoritmų konvejeris su EKoG duomenimis, siekiant sukurti klasifikatorių, kuris atskiria skirtingų pacientų rankų ir liežuvio judesius. Daugiausia dėmesio skiriama konvoliucinio neuroninio tinklo modeliams. Tikrinama hipotezė, ar motorinių vaizdų klasifikatorius gali būti apmokytas naudojant realius motorinius duomenis, nes tokius duomenis lengviau surinkti. Apmokant modelius pagal skirtingus duomenų rinkinius, parodoma, kad motorinio aktyvumo duomenis lengviau atskirti, lyginant su motorinių vaizdinių duomenimis. Parodyta, kad spektrinės galios požymiai yra informatyvesni, lyginant su laiko požymiais. Galiausiai modelis naudojamas motoriniams vaizdiniams prognozuoti greitų akių judesių miego metu.

APPENDICES

A.1 Electrode positions per patient

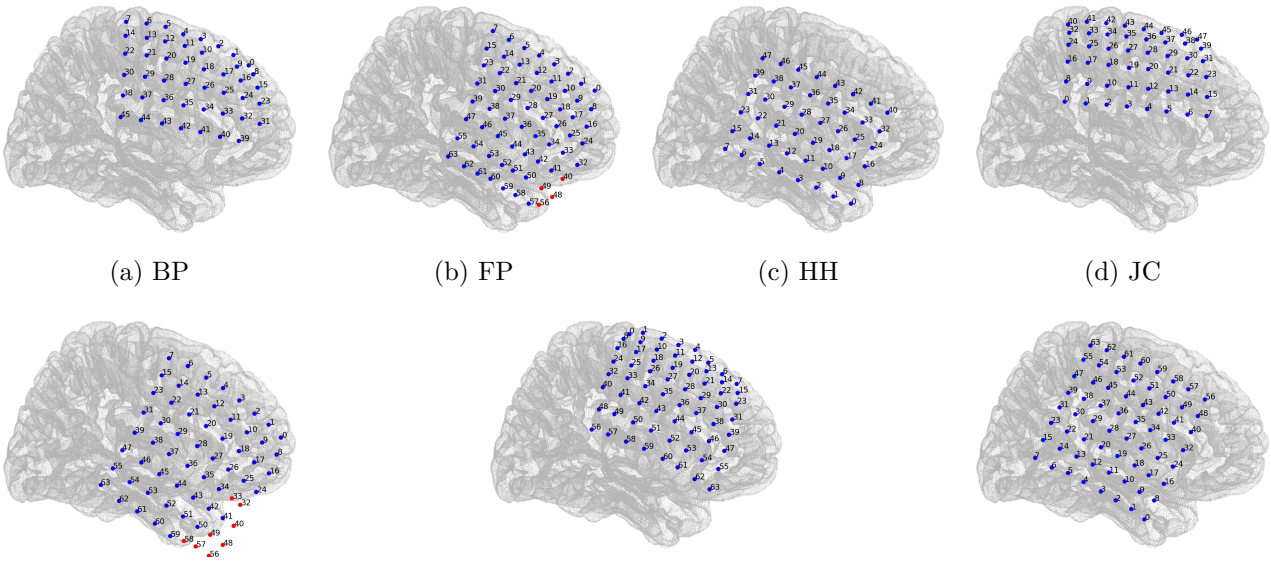

(a) BP (b) FP (c) HH (d) JC

(e) JM (f) RH (g) RR

Figure A.1: Electrode positions for each patients, numerated in the same order they appear in data. In all electrode position visualizations, red dots indicate electrodes which are projected badly into the standardized brain ("floating" in space rather than lying on the brain surface). Such electrodes are only for patients FP and JM. Blue dots indicate electrodes which look like correctly placed.

A.2 Activation map visualization

In all activation maps, red color means increased activation during task compared to the rest right after the task, while blue color means decreased activation. The mostly decreased activation in low frequencies and increased activation in high frequencies is consistent with Miller et al. (2010) findings that during both motor action and motor imagery tasks, there is decrease in 8 - 32 Hz power and increase in 76 - 100 Hz power (the sign of local cortical processing).

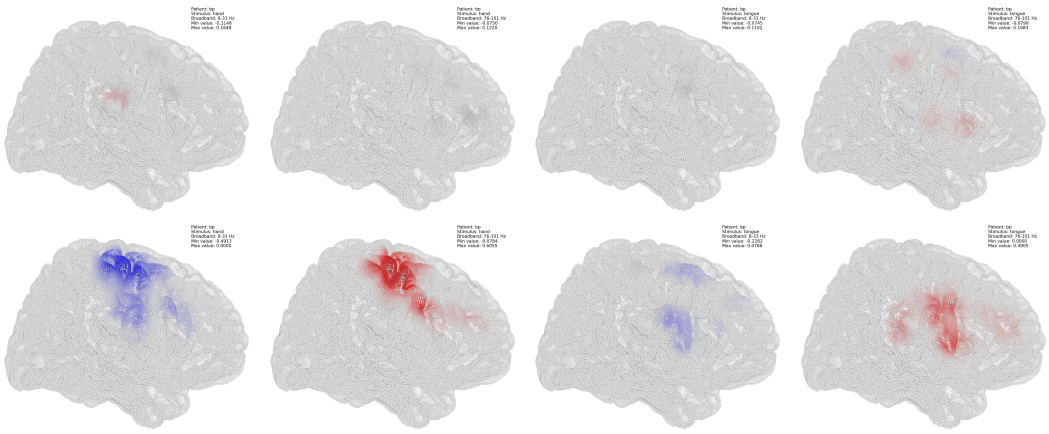

Figure A.2: Activation maps for BP patient

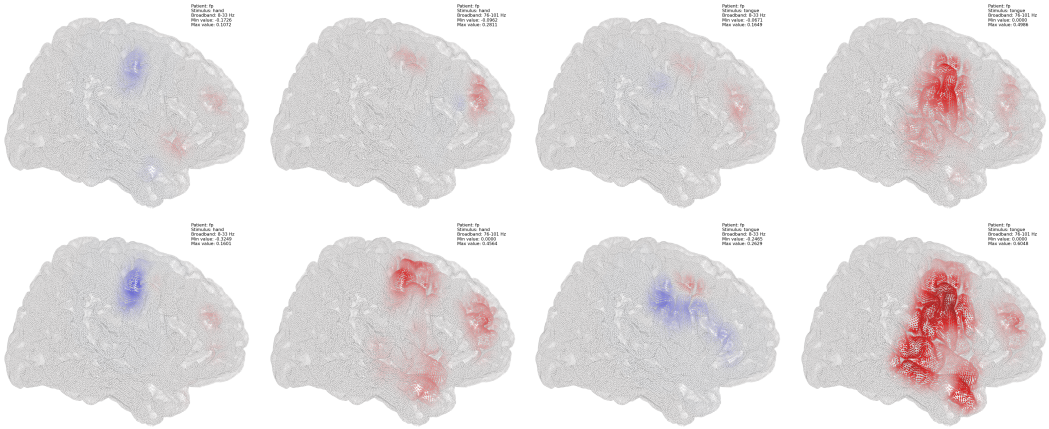

Figure A.3: Activation maps for FP patient

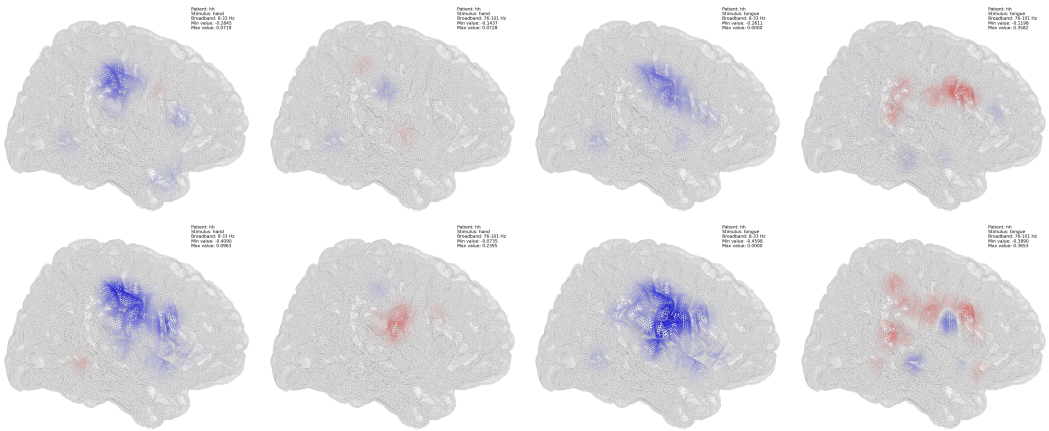

Figure A.4: Activation maps for HH patient

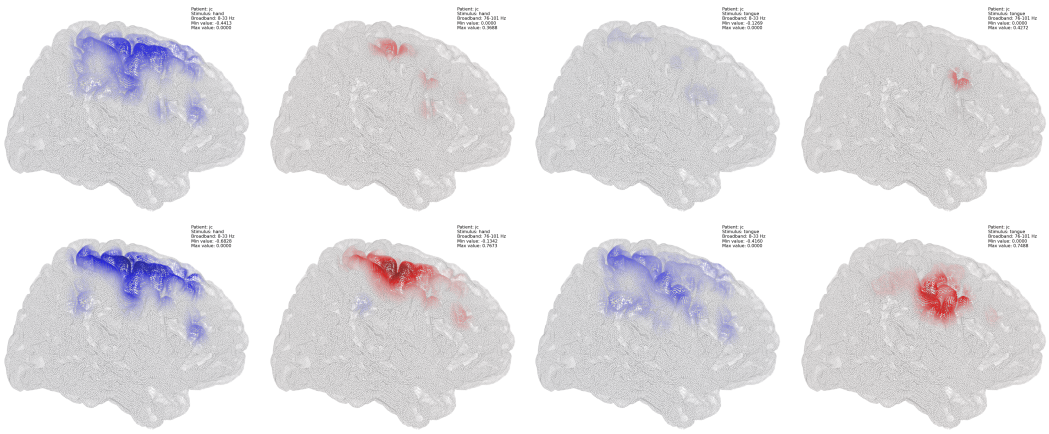

Figure A.5: Activation maps for JC patient

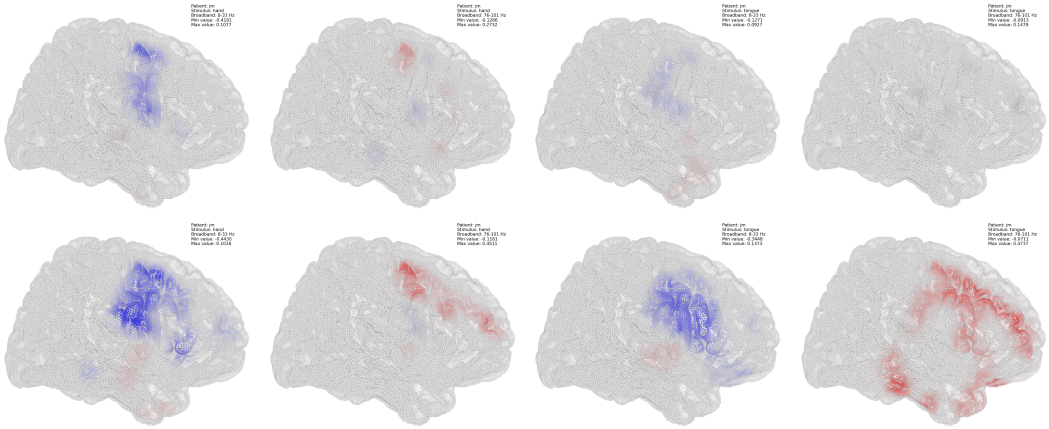

Figure A.6: Activation maps for JM patient

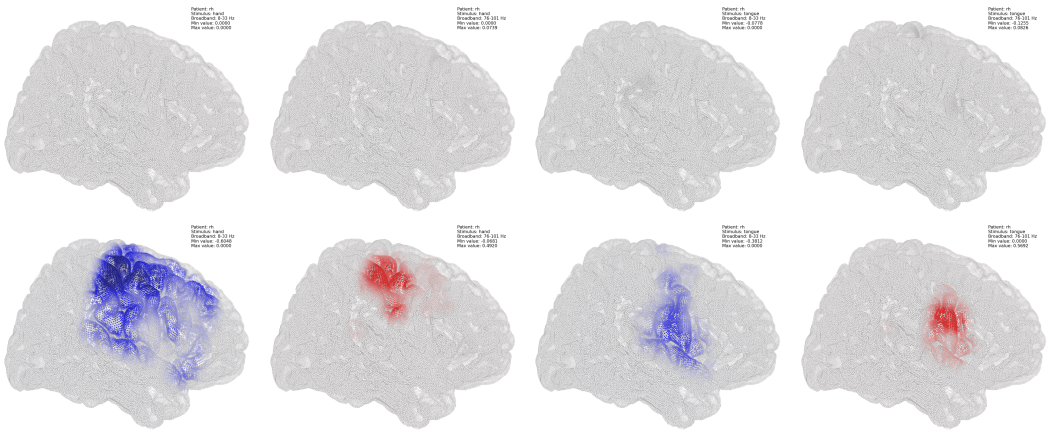

Figure A.7: Activation maps for RH patient

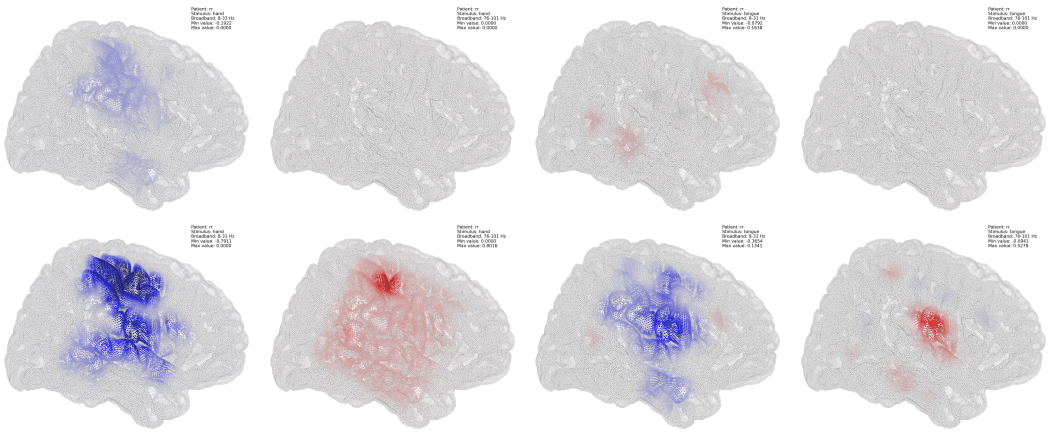

Figure A.8: Activation maps for RR patient

A.3 Visualization of model weights

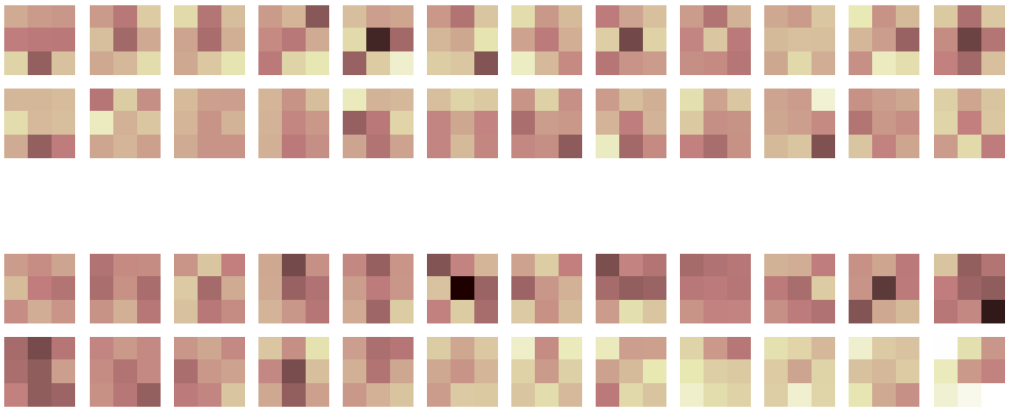

(a) RR, power-only, trained on motor action, accuracy = 77 %

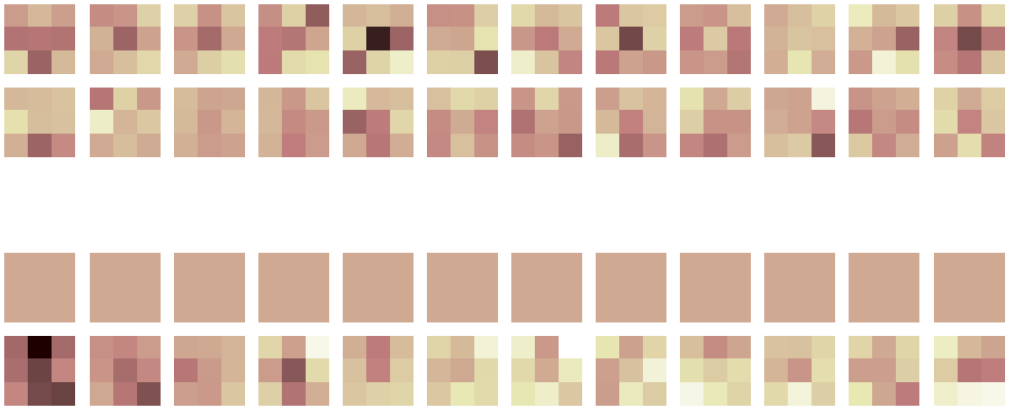

(b) BP, power-only, trained on motor action, accuracy = 74 %

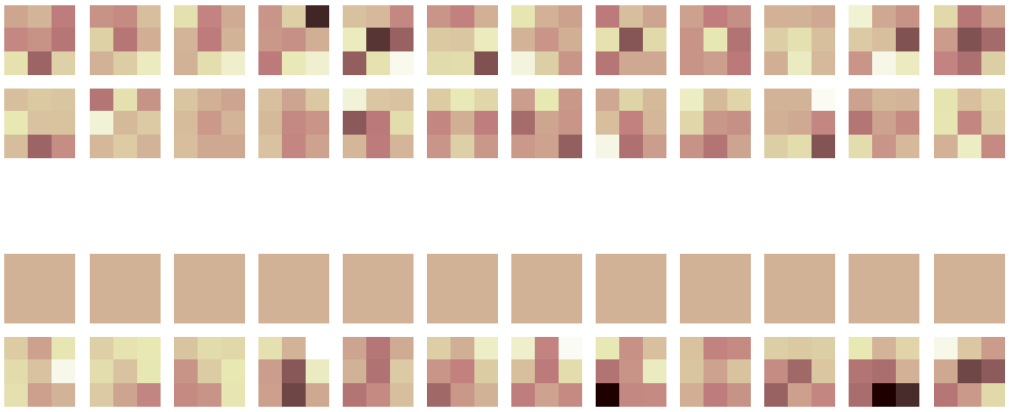

(c) HH, power-only, trained on motor action, accuracy = 50 %

Figure A.9: CNN layer weights after 50 training epochs for three models with different accuracy results. This CNN layer was oriented on spectral features. Darker color indicates higher values. Kernels in the top two rows were used on lower frequencies, and kernels in the bottom two rows - on higher frequencies. From left to right, each kernel correspond to a frequency band of 2 Hz width: 8 - 9 Hz, 10 - 11 Hz, ... , 30 - 31 Hz in the top two rows, and 76 - 77 Hz, 78 - 79 Hz, ... , 98 - 99 Hz in the bottom two rows.

A.4 Example REM sleep fragments with predicted movement classes

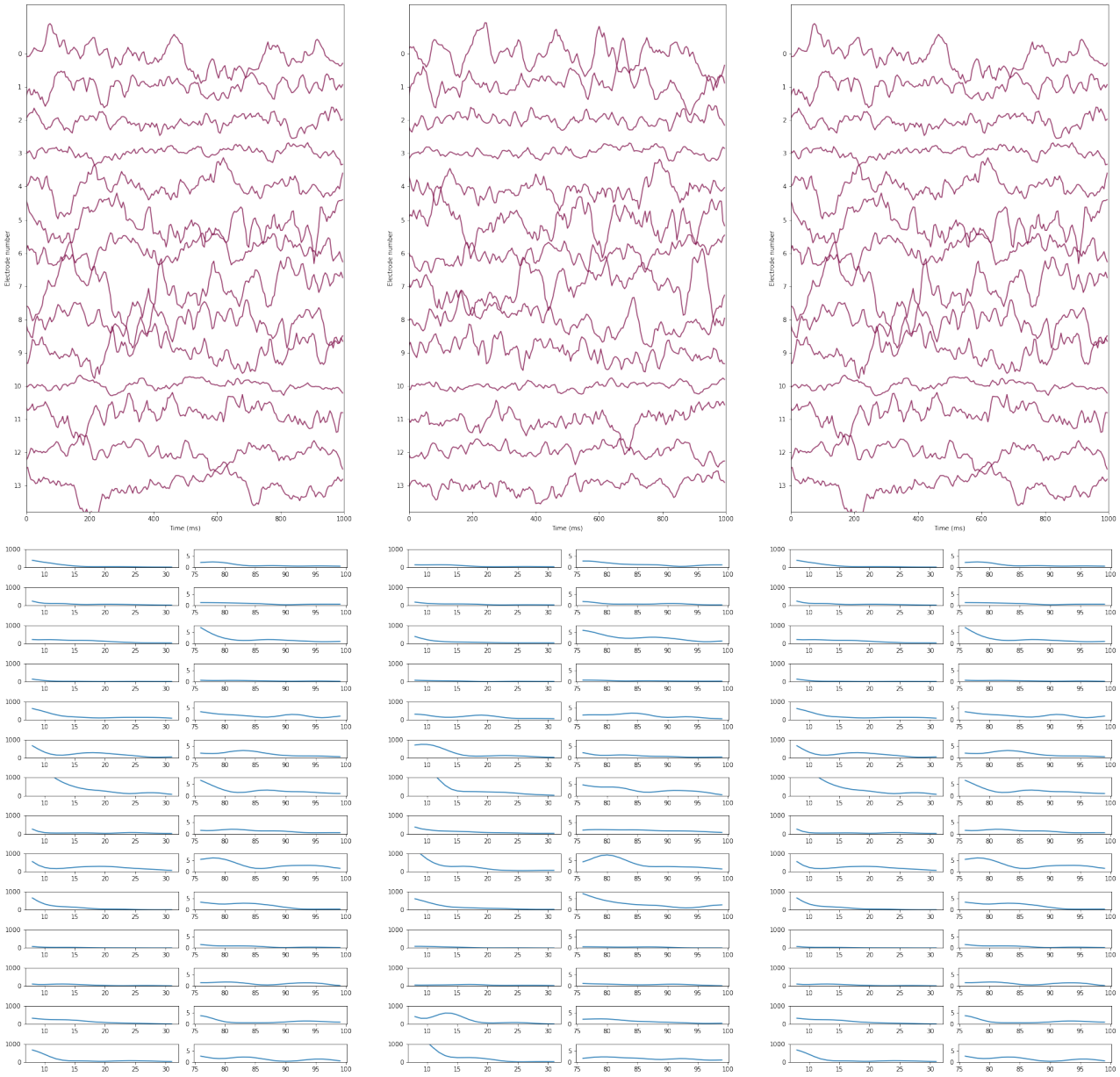

(a) “hand” motor imagery (b) “hand” motor imagery (c) “rest”

Figure A.10: Examples of REM sleep data fragments from patient nr. 106. Top row shows temporal fragment representation, bottom row shows extracted each electrode’s power in frequencies of interest. First two fragments were predicted as having imaginary hand movements by four power-only models; the last one was predicted as “rest” by six power-only models.